



HAL
open science

The effect of surface heat fluxes on interannual variability in the spring onset of snow melt in the central Arctic Ocean

Elena Maksimovich, Timo Vihma

► **To cite this version:**

Elena Maksimovich, Timo Vihma. The effect of surface heat fluxes on interannual variability in the spring onset of snow melt in the central Arctic Ocean. *Journal of Geophysical Research. Oceans*, 2012, 117, 10.1029/2011JC007220 . hal-04115395

HAL Id: hal-04115395

<https://hal.science/hal-04115395>

Submitted on 4 Jun 2023

HAL is a multi-disciplinary open access archive for the deposit and dissemination of scientific research documents, whether they are published or not. The documents may come from teaching and research institutions in France or abroad, or from public or private research centers.

L'archive ouverte pluridisciplinaire **HAL**, est destinée au dépôt et à la diffusion de documents scientifiques de niveau recherche, publiés ou non, émanant des établissements d'enseignement et de recherche français ou étrangers, des laboratoires publics ou privés.

Copyright

The effect of surface heat fluxes on interannual variability in the spring onset of snow melt in the central Arctic Ocean

Elena Maksimovich¹ and Timo Vihma²

Received 21 April 2011; revised 25 May 2012; accepted 25 May 2012; published 14 July 2012.

[1] The timing of spring snow melt onset (SMO) on Arctic sea ice strongly affects the heat accumulation in snow and ice during the melt season. SMO itself is controlled by surface heat fluxes. Satellite passive microwave (SSM/I) observations show that the apparent melt onset (MO) varies a lot interannually and even over 50–100 km distances. The MO record appeared to be a complex blend of SMO on top of sea ice and opening of leads and polynyas due to divergent sea ice drift. We extracted SMO out of the original MO record using sea ice concentration data. Applying ERA Interim reanalysis, we evaluated the portion of SMO variance explained by radiative and turbulent surface heat fluxes in the period of 1989–2008. The anomaly of the surface net heat flux 1–7 days prior to SMO explained up to 65% of the interannual variance in SMO in the central Arctic. The main term of the net flux was the downward longwave radiation, which explained up to 90% of SMO variance within the western central Arctic. The role of the latent and sensible heat fluxes in earlier/later SMO was not to bring more/less heat to the surface but to reduce/enhance the surface heat loss. Solar radiation was not an important factor alone, but together with other fluxes improved the explained variance of SMO. Local 20-year SMO trends averaged over the central Arctic Ocean are toward earlier melt by 9 days per decade.

Citation: Maksimovich, E., and T. Vihma (2012), The effect of surface heat fluxes on interannual variability in the spring onset of snow melt in the central Arctic Ocean, *J. Geophys. Res.*, 117, C07012, doi:10.1029/2011JC007220.

1. Introduction

[2] The melt season on Arctic sea ice is short, typically about 2–4 months (May–August), with the most intense incident solar shortwave (SW) radiation during May–July of 150–300 W/m² (daily means) at the surface [Ebert and Curry, 1993]. Prior to the melt onset (MO) on top of compact sea ice, the snowpack is dry and reflects 80–90% of the incident SW radiation. With MO, free water appears within the snowpack and snow crystals coarsen. As a result, SW scattering within the snowpack weakens and SW absorption increases [Grenfell and Perovich, 1984, 2004]. Therefore, an earlier snow melt by a few days increases the accumulation of SW radiation within the snowpack, which makes an important contribution to the total surface heat storage during the melt season [Bitz *et al.*, 1996]. Radiation measurements in the central Arctic have quantified that one day earlier MO on top of the sea ice increases the melt season cumulative absorbed SW energy at the sea ice - ocean surface by approximately 8.7 MJ/m², corresponding to the

additional 3 cm of summer ice melt [Perovich *et al.*, 2007b]. In comparison, 1-day delay in fall freeze-up results in an increase by only 1.5 MJ/m², or less than 0.5 cm of additional ice melt. An early MO on sea ice and the associated early generation of open water areas favor heat accumulation in the upper ocean [Drobot, 2007; Eicken and Lemke, 2001; Perovich *et al.*, 2007a]. Further, it takes more time in autumn to cool warmer water masses down to the freezing point. As a result, the freeze-up starts later, which contributes to sea ice thinning in the following year [Laxon *et al.*, 2003].

[3] Over the past few decades a tendency toward earlier MO in the Arctic has been revealed based on satellite observations. Already Anderson and Drobot [2001] have detected significant trends (1979–1998) toward earlier MO in the western central Arctic (8.9 days per decade), Lincoln Sea (4.4 days per decade) and Beaufort Sea (5.1 days per decade). Belchansky *et al.* [2004] evaluated the difference between two decadal averages (1979–1988 and 1989–2001): by 5 days in the Kara - northern Barents and Chukchi Seas, by 9 days in the East Siberian Sea, and by 4 days in the central Arctic. More recently, also based on a satellite passive microwave record, Stroeve *et al.* [2006] and Markus *et al.* [2009] demonstrated statistically significant 29-year (1979–2007) MO trends by 2–4 days per decade in the central Arctic, Laptev, East-Siberian, Chukchi and Beaufort Seas and the Baffin Bay. The tendency toward earlier MO and sea ice thinning [Giles *et al.*, 2008; Kwok and Rothrock, 2009] are essential elements in the recent Arctic warming,

¹Laboratoire d'Océanographie et du Climat: Expérimentation et Approches Numériques, Paris, France.

²Finnish Meteorological Institute, Helsinki, Finland.

Corresponding author: E. Maksimovich, Laboratoire d'Océanographie et du Climat: Expérimentation et Approches Numériques, 4, place Jussieu, Tour 45-55, Paris CEDEX 05, France. (maksimovich.elena@gmail.com)

but, according to our knowledge, reasons for the statistically significant 20–30-year trends in MO have not been explained yet.

[4] Trends as well as the interannual and regional variations in snow MO on top of sea ice are controlled by the surface heat fluxes. The surface fluxes, in turn, are affected by the air temperature and humidity, wind speed, clouds, snow and ice thickness, and the heat conductivity of snow and ice. By *surface* fluxes we mean the fluxes in the uppermost ~ 0.2 m of the snowpack. SW radiation penetrates into the snowpack, so that melt often starts a few cm below the surface [Cheng *et al.*, 2006, 2008]. An early (late) snow MO on top of sea ice is only due to an early and fast (late and retarded) net heat flux accumulation.

[5] Previous studies on the factors controlling the spring snow MO on sea ice have mostly addressed the role of a large-scale atmospheric circulation on the regional average MO, or the local effect of radiative and turbulent surface heat fluxes observed during field campaigns. Field observations by Barber *et al.* [1994], Granskog *et al.* [2006] and Vihma *et al.* [2009] demonstrated the importance of synoptic-scale variations and the diurnal cycle in the surface heat fluxes. Cheng *et al.* [2008] showed that success in modeling of snow MO strongly depends on the vertical resolution applied: with a 15–20 layer snow model resolving the snow MO better than a 3 layer model. The study by Yackel *et al.* [2007] indicated on a poor agreement (no significant relationship) between the near-surface air temperatures (daily means reaching 0°C) and the remote sensed MO on sea ice.

[6] Drobot and Anderson [2001] and Belchansky *et al.* [2004] both developed algorithms for MO detection by remote sensing and found that interannual variations in the regional mean MO within the Arctic are affected by the large-scale atmospheric circulation (the Arctic Oscillation index) and the near-surface air temperatures (SAT) during preceding months. The role of clouds and atmospheric moisture content in snow MO timing on sea ice has been addressed by Zuidema *et al.* [2005], Stone *et al.* [2005], and Nghiem *et al.* [2003], but only a few direct investigations of the cloud radiative forcing on snow MO have been made [Zhang *et al.*, 1996, 1997], based on a radiative transfer model only. Little attention has been paid to small-scale spatial differences and interannual variations in the observed snow MO and surface fluxes.

[7] Our approach is totally different. We examine whether radiative and turbulent surface heat fluxes on top of Arctic sea ice (based on meteorological reanalysis) can explain the interannual and spatial (50–130 km scale) variations in snow MO (based on remote sensing retrievals) within a vast domain (83 – 87°N) and over a 20-year period (1989–2008). This kind of analysis requires (1) a distinct definition of what is regarded as snow MO, (2) an estimation of the relative importance of the individual surface fluxes (shortwave and longwave radiation as well as the turbulent fluxes of sensible and latent heat) and various combinations of fluxes in the further timing of snow MO, and (3) an evaluation of the length of a relevant pre-melt period when surface flux anomalies are crucial for further timing of snow MO.

[8] The three data sets utilized in this study are described in section 2: ERA Interim reanalysis of surface fluxes and two remote sensing records of (a) sea ice concentrations and (b) MO. As we will highlight, the satellite retrievals of MO

do not only represent the snow melt onset (SMO) on top of the compact sea ice, but also include cases of divergent sea ice drift. Hence, our first task was to extract the SMO signature from the original MO record. The methodology applied is outlined in section 3.1. To compare the SMO timing and the heat flux anomaly prior to SMO we introduce three alternative and complementary methods. At this stage we make assumptions on the relevant temporal and spatial scales of the processes (sections 3.2 and 3.3). 20-year climatologies of the original MO record and the extracted SMO sample are illustrated in section 4.1, and statistics of the surface heat flux components are presented in section 4.2. The main result of this study: the role of the surface fluxes in SMO variability is outlined in sections 4.3 and 4.4. 20-year tendencies in MO, SMO and surface fluxes are considered in section 4.5. The results and perspectives for future work are discussed in section 5, and the concise conclusions are drawn in section 6.

2. Data

2.1. Melt Onset Data

[9] The appearance of water in snow causes the grains to cluster, resulting in larger grains with a more rounded shape. As a result, the snow emissivity increases in the near-infrared and microwave wavelengths, and the reflectivity decreases in the visible spectrum. Field observations show that the initial surface melt is often followed by episodic refreezing and melting, each time affecting the emissivity and reflectivity of the surface [Barber *et al.*, 1994; Ehn *et al.*, 2006]. First attempts to detect MO with the help of satellite visible, near-infrared and microwave measurements date to 1980s [Anderson, 1987; Grenfell and Perovich, 1984; Robinson *et al.*, 1986]. It was soon found that cloud cover and precipitation have the strongest effect on the visual and near-infrared spectrum [Forster *et al.*, 2001; Yackel *et al.*, 2007], thus making the microwave observations the most compatible for MO detection. For this reason, the recently updated Arctic-wide MO record derived from the Scanning Multichannel Microwave radiometer and Special Sensor Microwave Imager (SMMR-SSM/I) passive microwave measurements of brightness temperature [Markus *et al.*, 2009] was chosen for our study. MO data set is available on <http://neptune.gsfc.nasa.gov/csb/index.php?section=50>.

[10] The MO spatial resolution (pixel size) is approximately 25 km with the northward limit at 87°N . Compared to the other time series, the major advantage of this MO record is that until recently it was the only one to cover the complete 30-year period of 1979–2008 and both multiyear and first-year ice areas.

[11] Markus *et al.* [2009] defined the MO as the first day of the continuous melt. Thus, at each individual 25 km pixel, the snow MO is the day of the year when water in liquid phase stays continuously present on top of sea ice (first-year or multiyear), either within the snowpack or on top of the bare ice. Otherwise, if no clear snow MO signal is detected, the day when the sea ice concentration drops below 80% for the last time before the area (pixel) becomes ice-free, is considered as MO. It means that formation of open water areas (leads and polynyas) is also included in the MO record, although leads and polynyas may open without any melt, but only due to divergent sea ice drift.

[12] This MO retrieval has been compared by *Markus et al.* [2009] with buoy observations of surface air temperature (SAT) and reanalysis data from the National Center for Environmental Prediction and the National Center for Atmospheric Research (NCEP/NCAR). At two locations (one multiyear and the other with first-year sea ice) SSM/I-based and SAT-based snow MO agree within less than 8 days (better over first-year ice). Over the entire Arctic Ocean these three MO estimates (SSM/I, buoy SAT and reanalysis SAT) were compared during one particular year in terms of their spatial distribution statistics. While spatial distribution curves do not perfectly mirror one another, they are in a very good agreement. This comparison, however, does not provide the conclusive quantitative validation for the SSM/I-based snow MO retrievals. First, because SAT data (both buoy observations and reanalysis) themselves have errors. Second, because melt within the snowpack does not necessarily coincide with 0°C or -1°C air temperatures at 2 m height [Yackel *et al.*, 2007]. Third, because when varying the threshold applied to SAT data by $\pm 2^{\circ}\text{C}$, the resulting SAT-based MO ranges by as much as ± 50 days [Markus *et al.*, 2009].

2.2. Sea Ice Concentration

[13] We utilized a daily Arctic sea ice concentration (SIC) record by *Cavaliere et al.* [1996], which is based on the same SMMR-SSM/I brightness temperature measurements with the same spatial resolution as the MO data. These SIC data were produced with the NASA Team Algorithm and obtained from the National Snow Ice Data Center website <http://nsidc.org/data/nsidc-0051.html>. Note that in the algorithm for the MO detection developed by *Markus et al.* [2009] the same NASA Team Algorithm was applied for SIC estimation.

2.3. ERA Interim Reanalysis Data

[14] ERA Interim reanalysis (ERA-I) of the surface heat fluxes with 12 h intervals [Dee *et al.*, 2011] were chosen for the comparison with the MO record. ERA-I is the newest of the three reanalyses produced by the European Centre for Medium-Range Weather Forecasts (ECMWF). ERA-I has a global coverage with a spatial resolution of 0.72° latitude by 0.72° longitude, spanning the period from 1989 onwards. ERA-I benefits from the experience of previous reanalyses, with several major improvements: higher resolution, assimilation of more extensive and diverse observational data with a more sophisticated technique (four-dimensional variational data assimilation), an improved hydrological cycle and a variational bias correction of satellite radiance data [Dee and Uppala, 2009]. Compared to the earlier ERA-40 reanalysis, ERA-I also has a better vertical consistency of the air temperature in the Arctic region [Uppala *et al.*, 2008; Dee and Uppala, 2009]. This comparison was done against 2000 radiosonde reports inland north of 70°N . With the introduction of the variational bias correction in ERA-I, the vertical structure is now more efficiently constrained by radiosonde observations [Uppala *et al.*, 2008; Dee and Uppala, 2009].

[15] Over Arctic sea ice ERA-I vertical profiles of air temperature, humidity and wind have been validated against observations from three ship campaigns [Lüpkes *et al.*, 2010]. It was found that ERA-I overestimates the near-surface humidity and air temperature during summer,

whereas the near-surface winds in ERA-I are represented more accurately, with the differences increasing at higher altitudes but remaining less than 1 m s^{-1} . According to our knowledge, the accuracy of ERA-I surface fluxes on top of Arctic sea ice is yet to be validated.

[16] In ERA-I the SIC is prescribed in the same way as for ERA-40 prior to January 2002 [Fiorino, 2004]. From 1 January 2002 to 31 January 2009 ERA-I follows the ECMWF operational forecasting system [Thiébaux *et al.*, 2003]. Sea ice concentrations below 20% are set to 0%. South of 82.5°N , SIC in ERA-I is based on SSM/I passive microwave measurements, and northward from 83°N SIC is set to 100% [European Centre for Medium-Range Weather Forecasts (ECMWF), 2008a], although this is not realistic. Sea ice in ERA-I has a uniform thickness of 1.5 m and no snow cover on top [ECMWF, 2008b]. No data on snow or ice surface temperature are assimilated to ERA-I. In this formulation, the variability of the conductive heat flux through the ice and snow is limited and depends primarily on the atmospheric fluxes. Radiative and turbulent surface fluxes from ERA-I include downward longwave radiation (LWd), net longwave radiation (LWnet), downward shortwave radiation (SWd), net (absorbed) shortwave radiation (SWnet) and turbulent fluxes of latent (LE) and sensible (H) heat. Positive values represent heat flux to the surface.

3. Methodology

3.1. Determination of Snow MO

[17] Considering the definition of the continuous MO by *Markus et al.* [2009], the ice conditions may evolve as follows. During some period in spring, the ice field diverges and SIC reduces to less than 80% (even down to 0%) in a SSM/I pixel. Then the wind changes and due to sea ice drift, SIC temporarily increases back to values exceeding 80% in the given pixel. A few days/weeks later, the snow melt onsets on top of sea ice or divergent ice drift exposes open water within the same area. In this situation the MO algorithm by *Markus et al.* [2009] determines the continuous MO as the last drop in SIC (below the 80% threshold) before the area becomes ice free or as the last snow MO event on top of the compact sea ice.

[18] In nature when SIC stays high (100%) throughout the pre-melt period, surface fluxes (and meteorological conditions) affect SMO and not vice versa. To ensure that SIC was high throughout the pre-melt period, we first distinguish the MO cases (pixels and years) least affected by the SIC changes in the pre-melt period. For that we tested several SIC filters, where the MO pixel was considered to be a *snow MO pixel*, if the daily (or time averaged) SIC prior to the MO did not fall below some threshold (80, 85 or 95%; see below).

3.2. Evaluation of the Relevant Temporal and Spatial Scales

[19] Besides removing those MO pixels that have already experienced the drop in SIC prior to MO, the two data sets (MO and surface fluxes) also need to be converted to a comparable spatial resolution. A question arises: what is the sea ice area that is affected by the surface fluxes at a fixed grid location? A drifting sea ice floe is under the effect of the flux at a fixed grid cell only during some limited period of

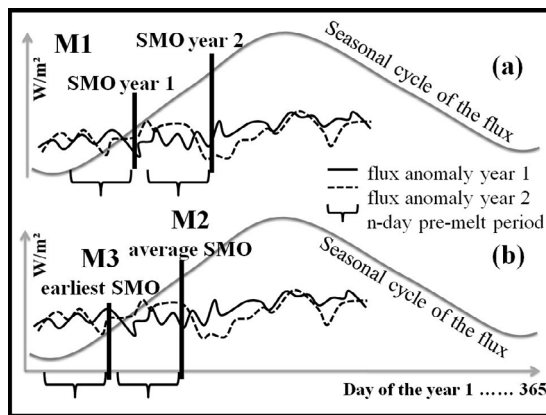


Figure 1. Schema of three methods (M1, M2 and M3) used to determine the pre-melt period and for calculation of the flux anomaly prior to SMO. In method M1 the pre-melt period is defined to start n days ($n = 1-40$) prior to the exact local SMO date, which varies both interannually and spatially. In methods M2 and M3 the pre-melt period varies spatially but not interannually. In M2 the pre-melt period starts n days before the local 20-year average SMO date, whereas in M3 the pre-melt period starts n days before the earliest local SMO during the 20-year period. The SMO date itself is not included in the n -day pre-melt period.

time. Before and after that, the ice slab is affected by surface fluxes at the neighboring grid cells.

[20] A comparison of different solutions led to the formulation of the following assumptions. Those MO pixels with a 40-day average SSM/I-based SIC $\geq 85\%$ during a 40-day pre-melt period were considered to be *snow MO pixels*. This 85% SIC filter allows for SIC changes in time, removing those pixels with a pronounced SIC reduction, and, at the same time, keeping those MO events least affected by SIC reduction already in the pre-melt period. Stronger SIC filters tend to reject most of the MO data set, which drastically reduces the study material. Snow MO timing in ERAI grid coordinates was determined as the average MO date of all *snow MO pixels* within a 130-km radius around each ERAI grid location. The radius is based on the following assumptions. With a typical wind speed of 5 m/s in spring, assuming that sea ice drift speed is 2% of the wind speed [Thorndike and Colony, 1982] and that the monthly displacement is half a trajectory length, the monthly ice displacement is approximately 130 km. This rough estimate agrees well with the satellite data on sea ice displacements (F. Girard-Arduin, IFREMER/LOS, personal communication, 2011). The monthly displacement naturally varies in space and time, but we only need an order of magnitude estimate to provide SMO spatial averaging.

[21] For clarity, we use the abbreviation SMO for the snow MO on sea ice and reserve the abbreviation MO for the melt onset as defined by Markus *et al.* [2009].

3.3. Comparison of SMO and Surface Fluxes

[22] We compared SMO data against ERAI daily surface heat flux anomalies (relative to the 20-year climatology) in the common 20-year period of 1989–2008. The very recent extension of ERAI for the period 1979–1988 became

available too late for this study. The flux anomalies were averaged over 1–40 days before a reference SMO date, and then compared to the SMO anomaly at the same location and year. Time averaging up to 40 days is demonstrated here, because it appeared that longer periods prior to SMO did not improve the capability of surface fluxes to explain the SMO timing. The definition of the reference SMO date and the further flux averaging were done using three alternative methods, schematically illustrated in Figure 1.

[23] With method M1 the flux anomalies were calculated right before the exact SMO date. As the SMO date is different each year and varies from one location to another, the variations in the reference date slightly hamper the interannual comparison of the flux anomalies. To fix the reference SMO date, we chose the 20-year average SMO date (method M2) and the 20-year earliest SMO date (method M3) at each location. This allows for a more suitable comparison of flux anomalies between different years, but the drawback is that the period just a few days before SMO is usually (M3) or in approximately half of the cases (M2) not included in the calculations.

[24] First order (bilateral) linear regression analysis was used to compare (correlate) two 20-year time series: the n -day average ($n = 1$ to 40) flux anomaly and the SMO anomaly, both in the same ERAI grid (Figure 2, example for the net flux). A statistically significant relationship with a 99% confidence level ($p < 0.01$) is established when the correlation coefficient (r) exceeds 0.56 ($r^2 > 0.31$). Over a compact sea ice cover, a causal effect of the surface flux anomaly on SMO requires a negative r : a positive flux anomaly precedes an early SMO and vice versa (Figure 2, example for the net flux). Considering the physical interpretation, r^2 represents the percentage of the interannual

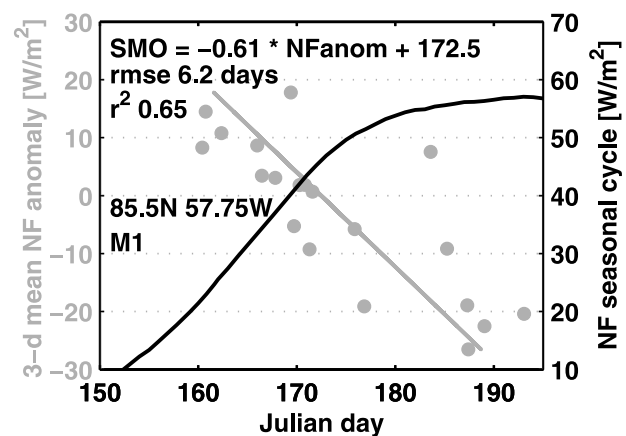


Figure 2. Causal relationship between a 3-day average NF anomaly and the corresponding SMO timing [Julian day] at one location 85.5°N 57.75°W. Black curve (right y axis) shows the 20-year mean seasonal cycle of NF at this location. Gray circles and their linear fit show the relationship between SMO (x axis) and the preceding NF anomaly (left y axis) averaged during 3-day pre-melt period prior to SMO (method M1). The linear regression equation suggests that a 3-day average local NF anomaly prior to exact SMO date explains 65% of the interannual local variance in SMO, with RMSE of 6.2 days.

variance in SMO timing explained by the interannual changes in the flux anomaly.

[25] Stepwise forward multiple linear regression analysis [Draper and Smith, 1998] was applied to find out how well various combinations of flux anomalies (LWd, SWd, LE and H) explain the interannual variance of SMO, and which combinations of ERAI fluxes best reflect SMO variability. Among 4 potential predictors (individual fluxes) the first term included in the multilinear regression equation correlates the best with SMO. At this stage we get a first-order linear regression equation. At the next step the predictor best explaining the residuals from the existing linear regression equation is accepted. This procedure is repeated further, as long as the correlation coefficient between the potential predictors and the residuals is significant. The overall multilinear regression equations (with 2, 3 or 4 terms) for each of 40 time averaging periods are examined for significance with an F test. The critical F -value depends only on a number of predictors included in the multilinear regression equation. Length of the time series is constant of 20 years, and $p < 0.01$. To note, the anomalies of all flux components included in the multilinear regression equation are averaged over the same time averaging period.

[26] In sections 2 and 3 we briefly described the MO algorithm developed and applied by Markus *et al.* [2009] to the daily brightness temperature measurements to evaluate the apparent MO at each 25 km pixel and each year (1979–2008). *Continuous* MO is considered here. However, usually some transition period characterized by alternating melting and re-freezing events occurs. During this period the daily amplitude in brightness temperature increases until it reaches a maximum in the beginning of the continuous melt [Markus *et al.*, 2009]. Time-space resolution of both data sets (SSM/I-based MO and ERAI fluxes) is limited. So it is evident that many of the localized (tens to hundreds of meters scales) episodic (of a few hours) snow melt events are not captured in either data set. From this point of view, it seems that the onset of *continuous* snow melt is a more distinct event than any *episodic* melt, and it should be better represented in both remote sensing records and meteorological reanalysis.

4. Results

4.1. MO and SMO Climatology

[27] According to the MO record produced by Markus *et al.* [2009], on average (in 1989–2008), the melt starts around late May at the southernmost ice margin: in the Greenland Sea, northern Barents Sea, southern Kara Sea, as well as Bering and Davis Straits (Figures 3a and 3b). The northward advance of melt from the Alaskan and Siberian coast and the northern Greenland Sea up to 87°N takes approximately 40 days (Figures 3a and 3b). The area farther north is unfortunately not covered by SSM/I observations.

[28] The analysis is complicated by the fact that MO timing is very variable in space (Figure 3e) and interannually (Figures 3c and 3d). In the central Arctic the MO differences over a 50 km distance are mostly less than 25 days (0.5 days km^{-1}), but there are some areas where the MO difference over a 50 km distance has even reached 3 months (2 days km^{-1} , Figure 3e). The majority of cases (pixel years) with the large horizontal MO gradients are due to early ice opening: lead and polynya formation already in March.

Accordingly, vast leads have occurred as far as 80–85°N. In the presence of compact (100%) sea ice cover, the regional differences in snow melt timing are controlled by the surface fluxes. Visual comparison of the MO maps with the surface fluxes on the Pacific side of the Arctic Ocean (70–85°N, 170–220°E) revealed a few large spatial gradients in heat fluxes across the areas of abrupt MO differences. Some of these differences in heat fluxes and MO seem to be associated to the atmospheric fronts, and not related to SIC changes (according to SSM/I-based SIC data). These MO events were, most likely, the true SMO cases. Yet, the episodic, short-lived (1–5 days) and highly localized spatial gradients in NF, SWd and H by up to 25 W/m^2 within a 50 km distance (between neighboring ERAI grid locations) do not convincingly explain SMO spatial gradients exceeding 1 month within a 50 km distance. Instead, the spatial differences in the ice type may provide an explanation for these pronounced MO gradients within totally ice-covered region. Field observations in April–May demonstrated that thinner sea ice is 5–10°C warmer at the snow-ice interface compared to thick ice [Perovich and Elder, 2001]. This is due to a larger conductive heat flux through thinner ice. Thus, with the same meteorological conditions and a uniform snow depth, on top of thin ice it takes less time to heat the snow to the melting point. In consequence, SMO starts earlier on top of thinner (initially warmer) ice floe, compared to thick multiyear ice.

[29] The typical local (same pixel) interannual fluctuations in MO are about ± 2 weeks around the average MO date in the central Arctic, increasing in the marginal seas, locally up to ± 4 weeks (Figure 3c). Application of the SIC filter to the original MO data, yielding the SMO sample (see section 3.2), reduced the local interannual variations and smoothed the spatial differences in the timing of surface melt initiation (Figures 3b and 3d).

[30] Figure 3f demonstrates the smallest one day SIC (SSM/I-based data of 25 km resolution) in a 40-day pre-melt period prior to MO (M1). Smallest SIC observed during 1989–2008 is shown for each 25 km pixel. As discussed already in section 3.1, our analysis reveals vast areas where SIC values have episodically fallen below 80% and sometimes even below 50% already before MO (Figure 3f). This means that already prior to continuous MO (divergent ice drift or snow MO) the reduced SIC has in some springs affected the surface heat fluxes, although not necessarily in ERAI.

4.2. ERAI Climatology of Surface Fluxes in April–June Within 83–87°N

[31] The ERAI fluxes least affected by SIC changes are those within the circumpolar Arctic between 83.25°N and 87°N, where the SIC in ERAI (but not in reality) is 100% every year during the entire pre-melt period. Hereafter we focus on this circumpolar central Arctic region which occupies an area of approximately $1.7 \times 10^6 \text{ km}^2$.

[32] SWd increases rapidly as the polar day progresses on average from $90 \pm 40 \text{ W/m}^2$ in April up to $250 \pm 70 \text{ W/m}^2$ in June (Figure 4a). Absorption of SW radiation (SWnet) enhances in spring (Figure 4b) due to increasing downwelling SWd radiation: from $20 \pm 10 \text{ W/m}^2$ in April to $75 \pm 25 \text{ W/m}^2$ in June, becoming the most efficient in July. In ERAI the monthly albedo of sea ice and open water are prescribed according to the seasonal means as determined by

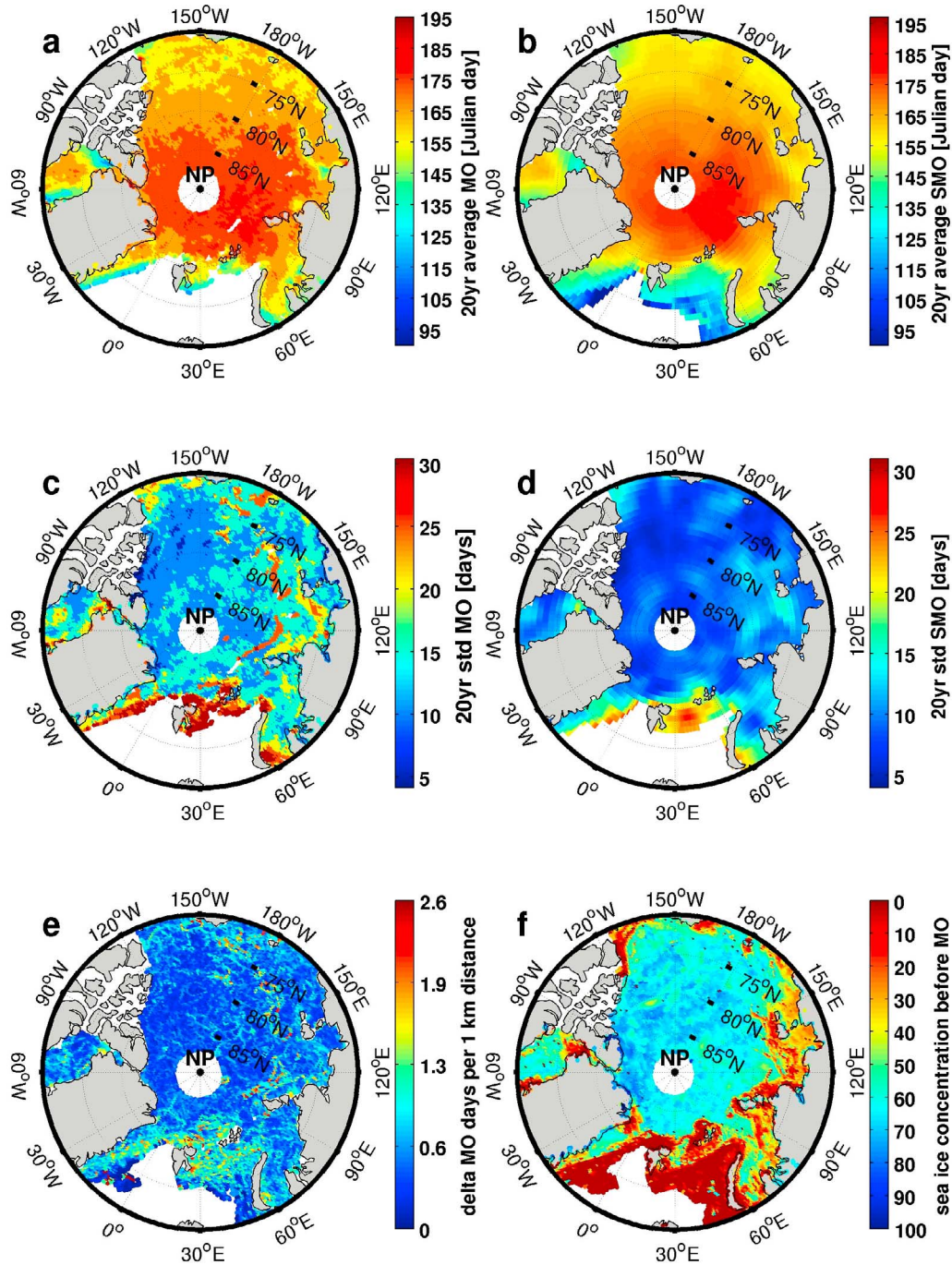


Figure 3. Maps of statistics of MO (SSM/I resolution of 25 km, based on *Markus et al.* [2009]), SMO (ERA-Interim grid resolution), and SIC (SSM/I) in the period 1989–2008: (a) 20-year average MO, (b) 20-year average SMO, (c) standard deviation of MO, (d) standard deviation of SMO, and (e) the largest differences in MO timing ever observed between two pairs of neighboring pixels (in the same year). These most extreme MO gradients were found in different years in different areas. (f) The smallest ever observed one day SIC in a 40-day pre-melt period prior to MO (method M1).

Ebert and Curry [1993]. The bare sea ice albedo value of 0.51 is taken as a representative value for summer, the dry snow albedo value of 0.77 is used for the winter months, and the open water albedo is approximately 0.06 [*Screen and Simmonds*, 2012].

[33] LWd is a major source of energy for the Arctic snow/ice surface all year-round. From April to June the air moisture

content increases, which promotes a larger LWd: of about $190 \pm 40 \text{ W/m}^2$ in April, reaching $290 \pm 30 \text{ W/m}^2$ in June (Figure 4c). Throughout the year, on average, there is a persistent surface radiative cooling in the central Arctic, with the negative net longwave radiation LW_{net} values (Figure 4d). Heat loss by means of LW_{net} reduces in spring from $40 \pm 25 \text{ W/m}^2$ in April to $25 \pm 20 \text{ W/m}^2$ in June (Figure 4d).

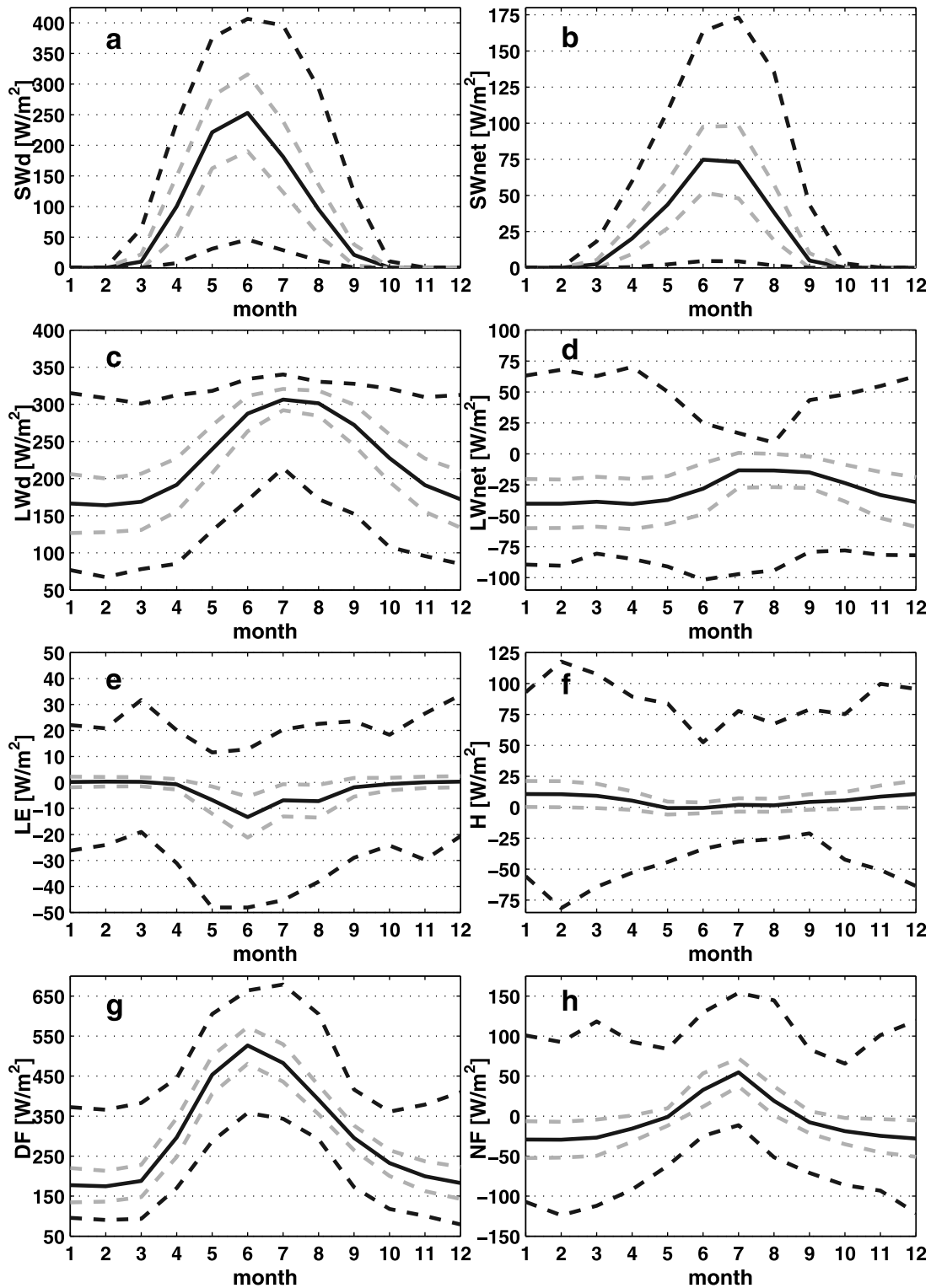


Figure 4. Seasonal cycle of ERAI surface fluxes within $83.25\text{--}87^\circ\text{N}$ in the period 1989–2008: (a) downward solar radiation SWd, (b) absorbed solar radiation SWnet, (c) downward longwave radiation LWd, (d) net longwave radiation LWnet, (e) latent heat flux LE, (f) sensible heat flux H, (g) downward flux DF, and (h) the net heat flux NF. The black solid curve is a 20-year average flux (grid-box area weighted). Two gray dashed curves delimit \pm one standard deviation of all daily values (in a given month) at all grid locations (within $83.25\text{--}87^\circ\text{N}$). Two black dashed curves delimit the maximum and minimum daily flux values ever occurred at any location (within $83.25\text{--}87^\circ\text{N}$) on any day of each month. Following ERAI convention, negative values correspond to surface heat loss (upward fluxes).

[34] The turbulent surface fluxes are on average relatively weak in spring, of the order of $\pm 20 \text{ W/m}^2$ [Ebert and Curry, 1993]. According to ERAI, sublimation of snow usually takes place during the pre-melt period, roughly April–May months (latent heat flux is upwards). In line with ERAI convention, the monthly and daily mean LE is represented by negative values in Figure 4e. Surface warming during May and early June results in a slightly unstable stratification near the surface, in both nature [Persson *et al.*, 2002] and ERAI. As a result, in May–June the monthly mean sensible heat flux is slightly negative (upwards), of the order of $2 \pm 2 \text{ W/m}^2$ (Figure 4f). The day-to-day variability in H and LE is about 5 W/m^2 and quite uniform regionally (not shown here).

[35] Downward radiation (DR) is the sum of LWd and SWd. Both LWd and SWd affect the local surface heat balance, but are not directly influenced by local feedbacks, such as changes in albedo and surface temperature. Although DR increases rapidly as the summer progresses (from 300 to 370 W/m^2 in April to 500 W/m^2 in June), the day-to-day variations are only 40 – 50 W/m^2 and rather uniform in space (not shown here). The downward flux (DF) is the sum of DR, H and LE (Figure 4g). Compared to DR, DF is more sensitive to surface properties (SIC and albedo) and small-scale processes (wind and near-surface thermal stratification). Nevertheless, over the sea ice the climatology of DR and DF is very similar. In spring DF increases rapidly: from $300 \pm 50 \text{ W/m}^2$ in April to $520 \pm 50 \text{ W/m}^2$ in June (Figure 4g).

[36] The net flux (NF) is the sum of LWnet, SWnet, H and LE. From August to May NF is negative on average, in the circum-polar central Arctic (Figure 4h). In spring the net surface heat loss switches to surface net heat gain, reaching $30 \pm 20 \text{ W/m}^2$ by June (Figure 4h). The local 40-day average NF prior to SMO (M1) is positive (10 – 15 W/m^2) in the circum-polar central Arctic (not shown).

4.3. Effect of the Surface Fluxes on the Interannual Variations in SMO

[37] After removing the MO pixels largely affected by the sea ice opening in the pre-melt period, methods M1, M2 and M3 were applied to calculate the time-average flux anomalies prior to the SMO date. Bilateral linear regressions were then calculated (at each grid cell) for the 20-year time series of SMO anomalies and corresponding surface flux anomalies. Results obtained with M1, M2 and M3 are qualitatively similar. Depending on the flux, one of the methods appears slightly better than the others. In this context, the best method (M1, M2 or M3) reveals the highest explained variance (r^2). Moreover the best method evokes the relationship (significant r^2) between SMO anomaly and the corresponding heat flux anomaly over a larger area than the other two methods. Comparison of r^2 at various locations suggests that M3 was slightly better for NF (Figure 5g) and M2 for LWd (Figure 5h). To illustrate the main results of this study, we made a compromise by selecting method M1, which reveals a stronger relationship between SMO and both NF and LWd (Figures 5g and 5h).

[38] The local interannual SMO variance is well explained by the interannual changes in NF. The highest r^2 is found with a synoptic time averaging period of about 1–7 days (Figure 5a), explaining locally up to 55–65% (maximum $r^2 = 0.65$) of the interannual SMO variance (Figures 5a and 5e). Considering the entire area where significant r^2 is

detected (shaded area in Figure 5e), the 4-day average NF anomaly explains 28% of the total (spatial and interannual) variance in SMO (Table 1). These results indicate that a large portion of our data sample contains a stronger surface NF accumulation (positive NF anomaly relative to the climatology) before the anomalously early snow melt (negative SMO anomaly). And correspondingly, the anomalously weak NF accumulation and even NF loss (negative NF anomaly) are suggested by ERAI in those years and locations where SMO is retarded (positive SMO anomaly).

[39] Next we consider the flux intensity: how large are ERAI NF anomalies (during this optimum 1–7 day pre-melt period) in those locations and years where and when SMO occurred particularly early or late? More precisely: what are the magnitudes of SMO and NF anomalies within the domain where the relationship between SMO and NF is established (shaded area in Figure 5e)? Figure 5c illustrates a group of 20-year time series at different grid locations: (1) SMO anomalies and (2) corresponding 1–7 day average NF anomalies. All ERAI grid locations with a significant r^2 at any (1–7 day) time averaging period are regrouped in Figure 5c. On average, when SSM/I-based SMO occurs anomalously early, for example by 15–20 days, the 1–7 day mean NF anomaly (ERAI) just before SMO is positive of about 17 – 18 W/m^2 (Figure 5c). An equally large negative NF anomaly is related to SMO delayed by 15–20 days.

[40] Results obtained with three fairly similar methods (M1, M2 and M3) show that the magnitude of the time average flux anomaly and its impact on SMO timing strongly depend on the definition of the pre-melt period. Whereas M1 suggests a high correlation between SMO and brief NF anomalies, M2 and M3 fail to detect the synoptic-scale effect of NF on SMO. Thus with M1 the effect of 1–7 days NF anomalies is detected over the area of $372 \times 10^3 \text{ km}^2$, which represents 22% of the circumpolar central Arctic. Instead, M2 and M3 are better in detecting the areas where SMO correlates with the NF anomaly over the preceding 20–40 days: $340 \times 10^3 \text{ km}^2$ for M2, $216 \times 10^3 \text{ km}^2$ for M3, and only $109 \times 10^3 \text{ km}^2$ for M1 (not shown).

[41] Considering the individual flux components, LWd alone explains up to 90% of the local interannual SMO variance, although only over a small area (Figures 5b and 5f). Among different time averaging periods, the 1–7 day LWd anomaly (M1) seems to best reflect the local interannual SMO variance compared to longer LWd history (Figure 5b). Thus for a time averaging period of 8 days or more, the highest r^2 drops lower than that for a 1 day time scale (Figure 5b). Similar results emerge when considering the entire shaded area in Figure 5f (as a group of locations and years, without regional averaging). Within this area the anomalous local (ERAI resolution) 6-day average LWd before the SMO accounts for 27% of spatial and interannual variance in SMO (Table 1). Within the same area, on average, the 1–7 day mean LWd anomaly of $+25$ (-14) W/m^2 is followed by 15–20 days earlier (later) SMO (Figure 5d). Below we summarize the size of area with significant correlations between LWd flux and SMO anomalies (not shown in figures). The effect of 1–7 day average LWd anomaly (just before SMO) on SMO appears within $589 \times 10^3 \text{ km}^2$ with M1 (35% of the circumpolar Arctic), compared to the area of 277×10^3 and $192 \text{ km}^2 \times 10^3 \text{ km}^2$ with M2 and M3 respectively. Similar to NF, calculations with M2 reveal vast

areas where LWd flux anomalies averaged over a longer (20–40 days) pre-melt period reflect the interannual behavior of the SMO. Thus the effect of LWd anomalies during a 20–40 day pre-melt period on SMO is present over an area of 733×10^3 (with M2) and $339 \times 10^3 \text{ km}^2$ (with M1). That is

about 43% and 20% of the circumpolar central Arctic respectively. As for NF, the magnitude of the time-average LWd anomalies (which correlate with the SMO timing) depends on the definition of the pre-melt period. Using M1, LWd anomalies of about 20–40 W/m^2 during a 20–40-day

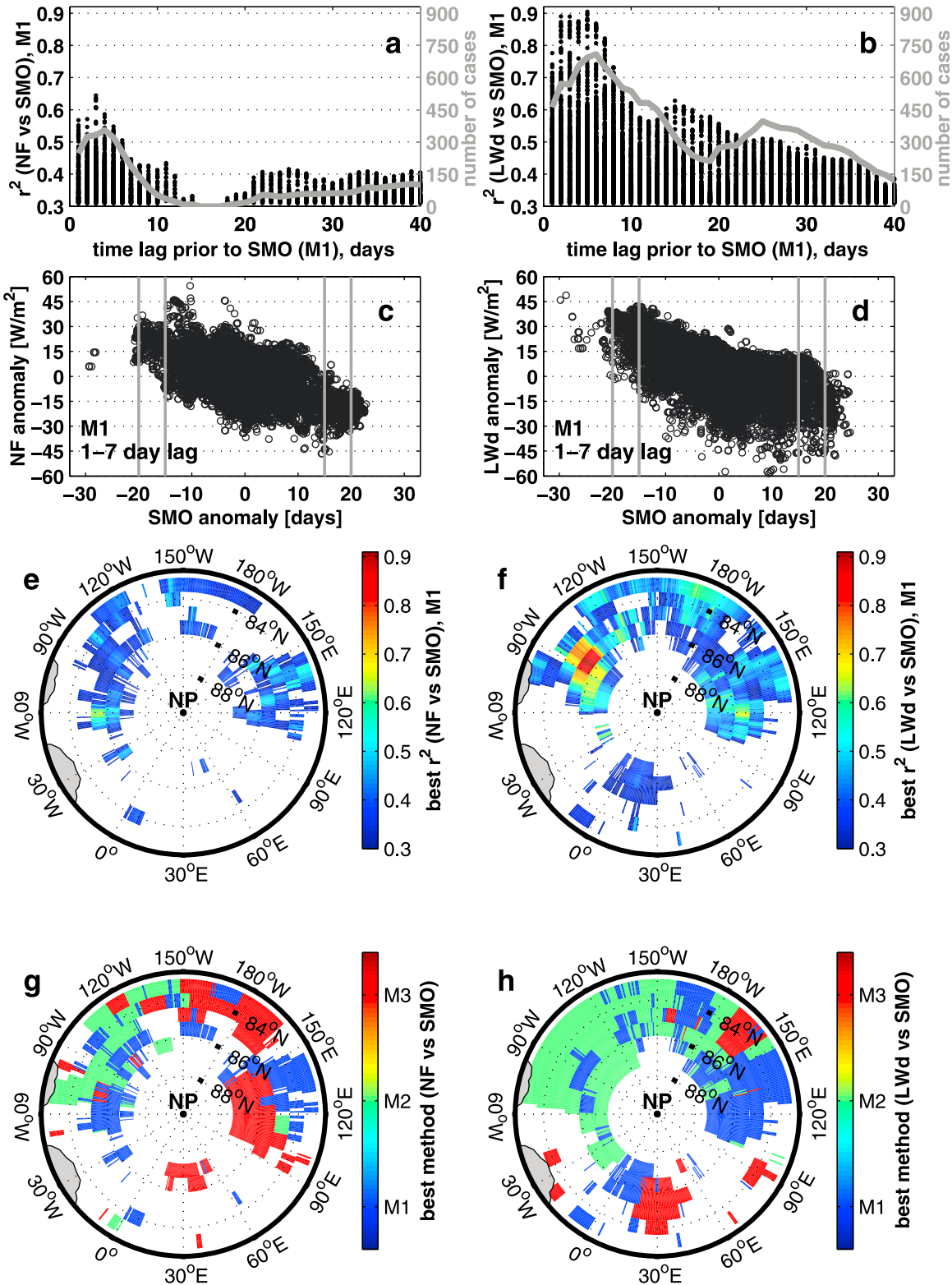


Figure 5

Table 1. Linear Relationships Between the Surface Heat Flux Anomaly (Prior to SMO) and SMO Anomaly Within the Circumpolar Arctic^a

Linear Regression Equation	Flux Averaging Period Prior to SMO (days)	r-Square	RMSE (days)	Area Where the Equation is Valid
$SMO = -0.38 \times NF + 0.03$	4	0.28	7.5	Shaded area in Figure 5e
$SMO = -0.35 \times LWd + 0.96$	6	0.27	7.3	Shaded area in Figure 5f
$SMO = -2.58 \times LE - 1.38$	40	0.31	7.3	Shaded area in Figure 6e
$SMO = -4 \times H - 0.68$	37	0.25	7.5	Shaded area in Figure 6f
$SMO = -0.31 \times LWd - 0.08 \times SWd - 0.67 \times H - 0.03 \times LE + 0.45$	5	0.18	7.7	Entire circumpolar area within 83.25–87°N

^aThe results presented are significant with $p < 0.01$. Bilateral regression analysis was applied to the combination of all those grid locations where at least one flux-averaging period suggests a significant relationship ($p < 0.01$) between a given flux and SMO (M1). The stepwise multi-linear regression equation (combination of LWd, SWd, LE and H) is valid for the entire circumpolar area within 83.25–87°N (M1). Depending on the flux (column 1), a certain n-day averaging period (column 2) yields the strongest relationship (column 3) between the corresponding n-day average flux anomaly and SMO. The strongest linear relationship has the highest r^2 compared to other flux-averaging periods (1–40 days prior to SMO). For example, the first line means that the 4-day average NF anomaly before the SMO date (M1) explains 28% of the total SMO variance (from year-to-year and between neighboring grid locations) with RMSE of 7.6 days. The stepwise multiple linear regression equation for the entire circumpolar central Arctic (83.25–87°N) ranks the contribution of individual heat fluxes in the equation.

pre-melt period affect SMO timing by as much as 18 days (not shown).

[42] The best results obtained with the three methods (M1, M2 and M3) are compared in Figures 5g and 5h. Within the colored domain at least one method and at least one time-averaging period evoke a statistically significant r^2 . All three methods detect the relationship between ERAI fluxes and SMO timing, complementing one another. None of the methods is much better than the other two.

[43] Very similar results are obtained for the LWnet flux (not shown): 1–7 day time scales are the most illustrative for the seasonal transition (r^2 up to 0.9), with a secondary peak at about 30-day lag (r^2 up to 0.6). We speculate that the effect of brief (1–7 day) flux anomalies on surface melt can only be distinguished if the heat fluxes and SMO are well captured in both data sets.

[44] Anomalies in LE and H are positive (negative) in the early (late) SMO years (Figures 6c and 6d). Seasonal 30–40 day flux anomalies in H and LE (M1) explain up to 72% and 56% of the local interannual SMO variance respectively (Figures 6a and 6b). Local LE and H flux anomalies within the shaded areas in Figures 6e and 6f respectively account for 31% and 25% of the spatial and interannual variance in SMO (Table 1). On average 1–2 W/m² weaker (stronger) loss of sensible heat and 2–3 W/m² weaker (stronger) loss of latent heat (sublimation) during May–June (30–40 day pre-melt period) contribute to the advance (delay) in SMO by 15–20 days (Figures 6c and 6d). A statistically significant effect of 30–40 day mean flux anomalies (M1) to SMO variance is found over the areas of 254×10^3 km² for LE and

300×10^3 km² for H (15% and 18% of the circumpolar Arctic). To note, these areas are only a part of the shaded domain in Figures 6e and 6f (where all time averaging periods are considered together). The performance of three methods (M1, M2 and M3) in terms of r^2 is compared in Figures 6g and 6h. Accordingly, LE and H flux anomalies computed with either M1 or M2 capture the interannual local variability in SMO better (with larger r^2) than M3.

[45] Our results show that SWd and SWnet (on their own) do not play any role in the interannual and/or spatial variability in SMO within the central Arctic (83–87°N). This is reasonable, as until mid-May the sea ice albedo in ERAI is rather high (0.77), and since there is no snow melt (and no ice melt) in ERAI, the representation of SWnet variations in time is unrealistic.

[46] The effect of DF and DR anomalies on SMO is weak: although the anomalies locally explain up to 50% of the interannual variance in SMO, a significant r^2 is found only for less than 2% of the circumpolar Arctic.

4.4. Effect of the Combination of Surface Fluxes on Interannual Variations in SMO

[47] Stepwise forward multiple linear regression analysis was applied to find those combinations of surface fluxes that best explain the SMO variance. Four predictors were taken into account: LWd, SWd, LE and H. These individual fluxes and various combinations of them are considered here as the direct factors controlling SMO.

[48] A combination of 2–4 fluxes explains locally from 30 to 92% of local interannual SMO variance within roughly

Figure 5. Bilateral regression results on the relationship between the flux anomaly and the corresponding SMO anomaly (same location, same year). The study domain is within 83.25–87°N. The flux anomaly is averaged over various pre-melt periods (1–40 days, method M1). Left-hand plots illustrate the results for NF and right-hand plots for LWd. (a, b) Dependence of the squared correlation (r^2) on the length of the pre-melt period. The black dots show all significant r^2 values ($p < 0.01$) for each flux-averaging period. The gray curve shows the number of ERAI grid locations where a significant r^2 was found with the given flux-averaging period. It indicates which time averaging period is the most successful in explaining interannual SMO variance. (c, d) Scatter of 1–7-day flux anomalies against corresponding SMO anomaly. All locations evoking a significant r^2 at any flux-averaging period between 1 and 7 days are regrouped. Each location is represented with 20 black open circles (20 years). Four vertical gray lines delimit ± 15 –20 day SMO anomalies. The average of 1–7 day flux anomalies corresponding to these ± 15 –20 day SMO anomalies is cited in the text. (e, f) The highest r^2 found with some of the flux-averaging periods (1–40 days), method M1. All grid locations where at least one significant r^2 was detected with M1 are shown. (g, h) Comparison of the highest r^2 ($p < 0.01$) obtained with the three methods (M1, M2 and M3) and all flux-averaging periods (1–40 days).

a half (46%) of the circumpolar central Arctic area (Figure 7a), with a root mean square error (RMSE) about 6–7 days (not shown). In the western central Arctic, within the area where 3–7 day average flux anomalies (Figure 7b) explain 80–90% of SMO variance (Figure 7a) at least 3

fluxes (Figures 7c–7f) appear in the multilinear regression equation, with LWd the dominating term (Figure 7c). Within another sector in the western Arctic, a 40-day time average (Figure 7b) LE and H are either the only or most important terms included in the best multilinear regression equation

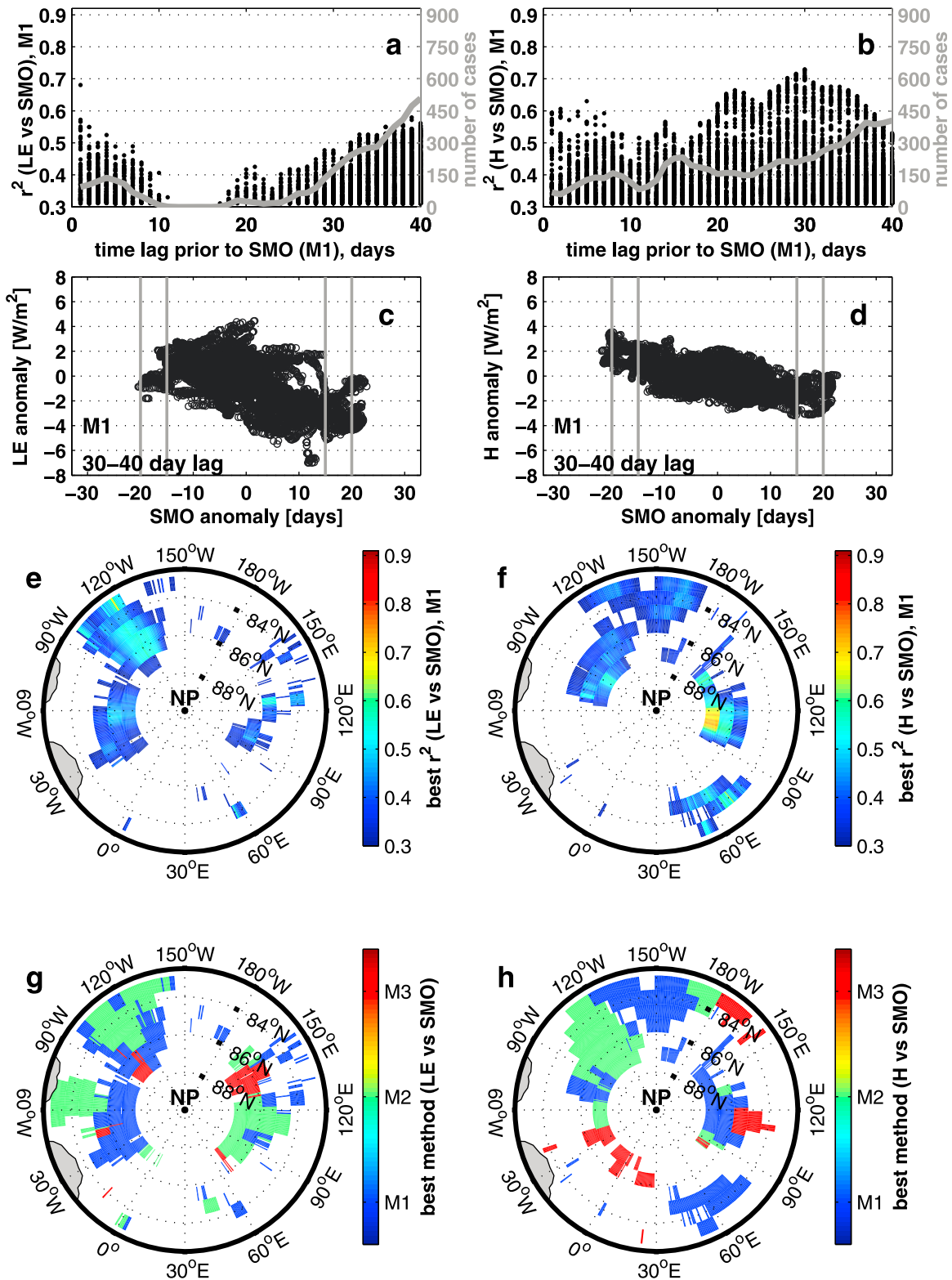


Figure 6

(Figures 7e and 7f). Interestingly, although SWd by itself does not correlate with SMO, the inclusion of SWd into the multilinear regression equation improves the explained variance of SMO over most of the central Arctic (Figure 7d).

[49] Figure 8 compares the best results obtained with the bilateral and multiple regression analysis. Over most of the central circumpolar Arctic (68% of the study domain, shaded area) a combination of fluxes explains SMO better than any of the individual fluxes (Figure 8c) or their sum. LWd largely dominates over the other fluxes within the Pacific and Atlantic sectors of the central Arctic (Figure 8c). The best time averaging period within the Atlantic sector is 25 days on average (Figure 8b). On the Pacific side the best time averaging period has two peaks at 4–7 and 20–27 days.

[50] Stepwise multilinear regression analysis was also applied to the composite of all maritime grid locations (2862 in total) within the circumpolar central Arctic. Calculated in this manner, the combination of 5-day average LWd, SWd, LE and H anomalies explains 18% of the total SMO variance, with a standard error of the linear regression model of about one week (Table 1). To note, the total variance includes both interannual and spatial variance. Figure 9 demonstrates how well the best multilinear regression equation (in Table 1) reconstructs the local SMO features in three years: 1990, 2003 and 2007. Year 2003 is illustrated as a typical year with the SMO close to the 20-year average (Figures 9c and 9d). Year 2007 is taken for comparison as the most famous for its unique sea ice conditions (Figures 9e and 9f). SMO in 1990 is shown in contrast to SMO pattern observed in 2007: with essentially opposite SMO anomalies (Figures 9a and 9b). Accordingly, the best combination of four fluxes well captures the spatial features of SMO (Figure 9), but cannot explain SMO anomalies larger than 15 days.

4.5. Trends

[51] We first focused on the local MO trend at those SSM/I MO pixels with a complete 20-year time series. Statistically significant ($p < 0.01$) trend is found within 83.400 km² (shaded locations in Figure 10a), that is only 5% of the circumpolar central Arctic area (83.25–87°N). Depending on the location, the MO tendency is toward earlier MO, ranging locally between –8 and –18 days per decade (Figure 10a). The average of these significant local (in 25 km resolution) MO trends is –13 days per decade.

[52] There are three major differences in our experimental setup compared to Markus *et al.* [2009]. (1) Central Arctic domain is defined differently. (2) Our study period is only 20 years long (1989–2008) against a 29-year period in the study by Markus *et al.* [2009]. (3) Our trend estimate is for

each individual 25 km MO pixel, whereas Markus *et al.* [2009] calculated the trend for the “annual areal average MO” within the central Arctic region. According to Markus *et al.* [2009] in the central Arctic the MO trend was about –2.5 days per decade (1979–2007) and our calculations for the same 29-year period confirm this result ($p < 0.01$).

[53] Area average 20-year trend in SMO sample within the circumpolar central Arctic is –8.8 days per decade (Figure 10b). These results nicely illustrate how different approaches produce very different trends in MO/SMO: by –2.5, –8.8 and –13 days per decade.

[54] Both the interannual variability and trends in SMO should, in principle, be explainable by interannual variability and trends in NF. In contrast, the interannual variability and trends in the apparent MO can be also related to the sea ice dynamics. To discuss a possible relationship between the trends in surface fluxes and trends in SMO, again we first need to define the reference period of the year when changes in fluxes might trigger a larger/smaller heat accumulation within a dry snowpack. In our example here we averaged the surface fluxes during a 30-day pre-melt period (21 April–20 May) every year and calculated the linear trend at each ERAI grid location (Figures 10c and 10f). Where the 21 May is the earliest local SMO found within the circumpolar central Arctic (83–87°N) in the period 1989–2008.

[55] In the period of 21 April–20 May ERAI SWd, SWnet, LWnet, H, DR and DF follow significant 20-year trends within a portion of the study area (83–87°N), but not everywhere in the circumpolar central Arctic (Figure 10). The largest trends are found for SWd, DF and DR: reaching +15–20 W/m² per decade north of Greenland and in the Lincoln Sea. Since DR and DF trends are very similar in magnitude and have the same spatial features, only DF is illustrated here (Figure 10e). H and LWnet trends are negative (Figure 10f), which seems to be a consequence of a larger SWd and SWnet in ERAI: where H, LWup and LWnet strengthen (heat loss) with an increased surface heating by means of SWd. NF, LWd and LE trends in the period 21 April–20 May are insignificant. DR and DF trends are large and appear within the most of the study area.

[56] In reality the trends in SMO and surface fluxes (NF) could partly be due to changes in sea ice and snow cover and partly due to evolution of meteorological conditions. Recent studies manifested a significant thinning of sea ice in the Arctic Ocean [Kwok and Rothrock, 2009]. We speculate that younger (saltier, thinner and warmer) ice should have impacted the true NF at the snow surface, and likely contributed to the observed advance of snow melt in the spring (SSM/I). An interesting aspect to be highlighted: in the areas

Figure 6. Bilateral regression results revealing the relationship between the flux anomaly and the corresponding SMO anomaly (same location, same year). The study domain is within 83.25–87°N. The averaging period for the flux anomaly ranges from 1 to 40 days prior to SMO (method M1). Left-hand plots illustrate the results for LE and right-hand plots for H. (a, b) Dependence of the squared correlation (r^2) on the flux-averaging period. The black dots show all significant r^2 values for each flux-averaging period. The gray curve shows the number of ERAI grid locations where a significant r^2 was found with the given flux-averaging period. (c, d) Scatter of 30–40 day flux anomalies against corresponding SMO anomaly. Each location is represented with 20 black open circles (20 years). All locations evoking a significant r^2 at any flux-averaging period between 30 and 40 days are regrouped. Four vertical gray lines delimit ± 15 –20 day SMO anomalies. The average of 30–40 day flux anomalies corresponding to these ± 15 –20 day SMO anomalies is cited in the text. (e, f) The highest r^2 found with some of the flux-averaging periods (1–40 days), method M1. All grid locations where at least one significant r^2 was detected with M1 are shown. (g, h) Comparison of the highest r^2 ($p < 0.01$) obtained with the three methods (M1, M2 and M3) and all flux-averaging periods (1–40 days).

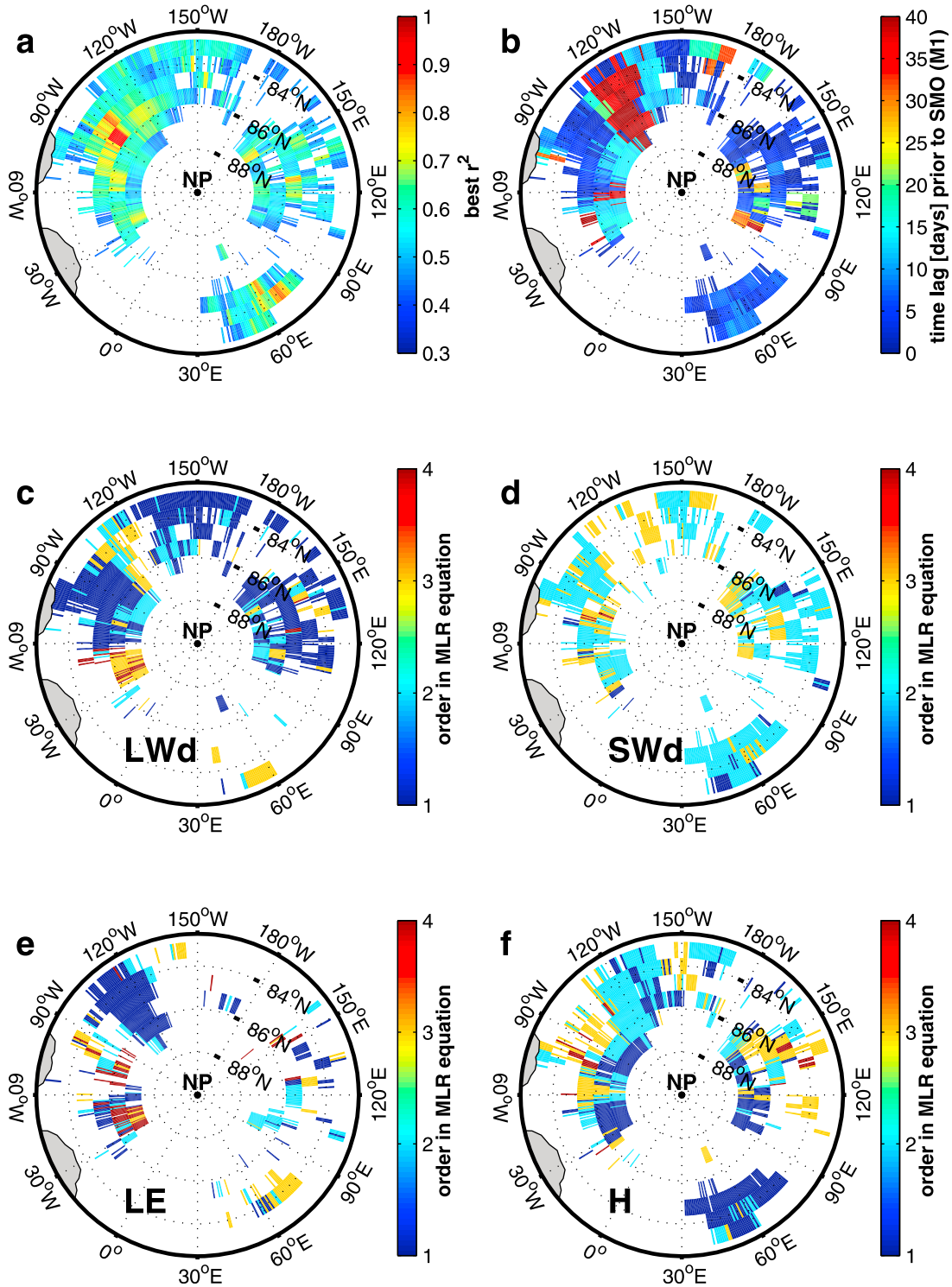


Figure 7. Best results for the stepwise multilinear regression (MLR) analysis at each individual grid location ($p < 0.01$), method M1. (a) Fraction of the local interannual SMO variance (r^2) explained by the best combination of four fluxes: LWd, SWd, LE and H. At each particular location r^2 value is the highest among all combinations of these four fluxes and 40 different flux averaging periods. (b) Flux averaging period suggesting the highest r^2 that results from the best combination of four individual fluxes. (c–f) Rank of the flux components in the best multilinear regression equation (at each individual grid location). For example, in Figure 7c at those locations where the color code refers to 1, LWd is the most significant flux component (with the smallest p -value) and the first included in the forward multilinear regression analysis.

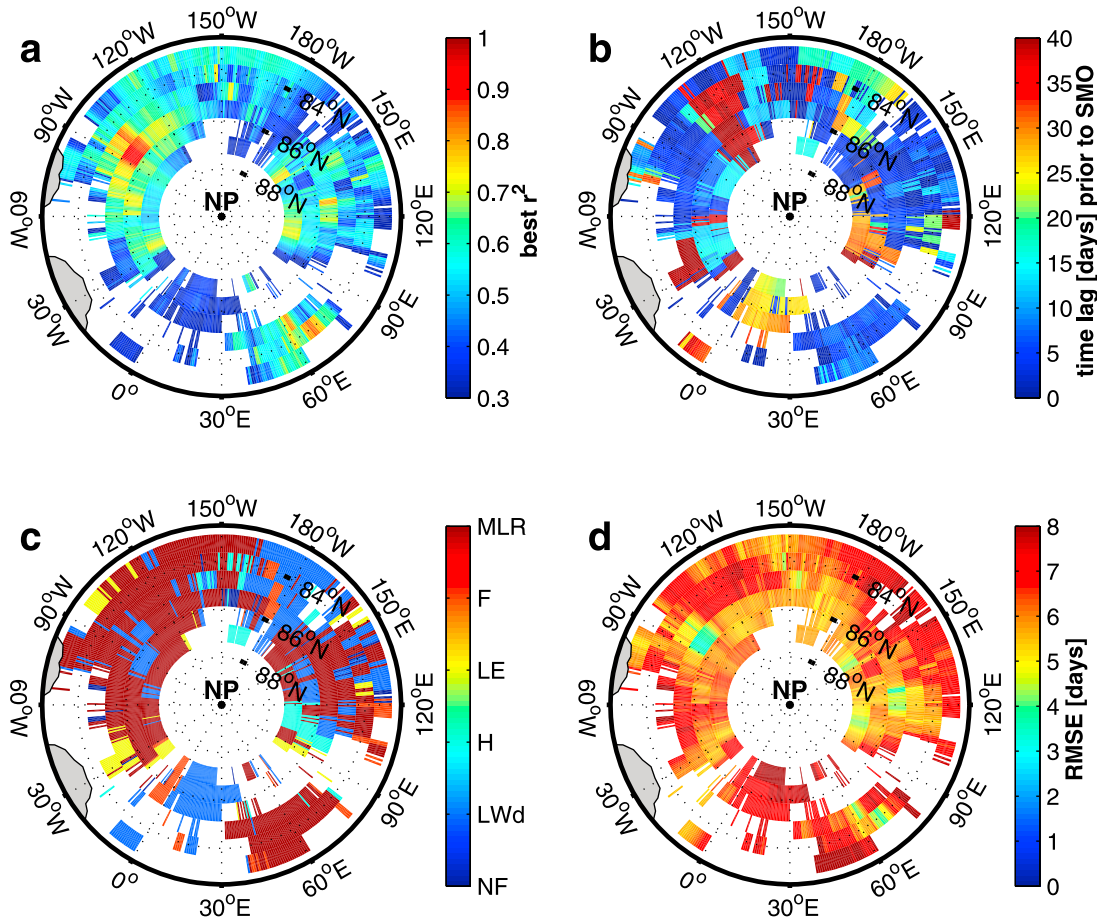


Figure 8. Comparison of the bilateral versus multilinear regression results, method M1. (a) Fraction of the local interannual SMO variance explained by the surface fluxes (r^2): NF, LWd, LWnet, SWd, SWnet, LE, H, DF, DR or any combination of 4 major fluxes (multilinear regression with LWd, SWd, LE and H flux components). At each particular location, this r^2 value is the highest among the individual heat fluxes, all combinations of four major fluxes and all flux averaging periods. (b) Flux averaging period suggesting the best r^2 that results from any individual flux or combination of individual fluxes at each grid location. (c) The factor best explaining SMO variance (individual fluxes or some combination of them, ranked by r^2) at each grid location. Multilinear regression (MLR) refers to some combination of LWd, SWd, LE and H flux anomalies, suggesting the best r^2 . Notation “F” corresponds to any of the following fluxes: NF, LWnet, SWd, SWnet, DF or DR. (d) RMSE corresponding to the best explaining factor shown in Figure 8c.

where the ice and/or snow have become thinner, a trend toward an earlier SMO might occur even with a negative trend in NF, LWd and SWd.

[57] The illustrated trends in surface heat fluxes are only based on ERAI, and not validated against observations. So far, the field spring-time flux measurements only exist for limited periods in a few ice stations. A strong debate has taken place on the reliability of trends in reanalyses (e.g. ERA-40) in areas where almost no observational data were assimilated, such as the central Arctic northward of 82°N [e.g., *Graversen et al.*, 2008; *Bitz and Fu*, 2008; *Grant et al.*, 2008; *Thorne*, 2008; *Screen and Simmonds*, 2011]. Although the reported magnitudes of trends differ among various data sets, all these cited studies agree that there have been warming trends in the central Arctic, in particular in spring and fall, with the earlier spring snow melt and later fall freeze-up. According to *Uppala et al.* [2008], *Dee and Uppala* [2009], and *Dee et al.* [2011],

ERA1 reproduces meteorological processes in the Arctic better than earlier reanalyses, which possibly has also improved the accuracy of radiative and turbulent fluxes on sea ice, but this is still an open question.

5. Discussion

[58] To successfully quantify the effect of surface fluxes on SMO, it was essential to take into account the following. First, instead of analyzing fluxes themselves, we paid attention to the flux anomalies relative to the 20-year climatology. Contrary to the flux anomalies, radiative fluxes themselves have a non-causal positive correlation with SMO: when SMO occurs late, corresponding seasonal values of LWd and SWd are larger. Second, we found that there is no single time scale for the pre-melt period when the contribution of surface fluxes to SMO is the most important. For NF, LWnet and

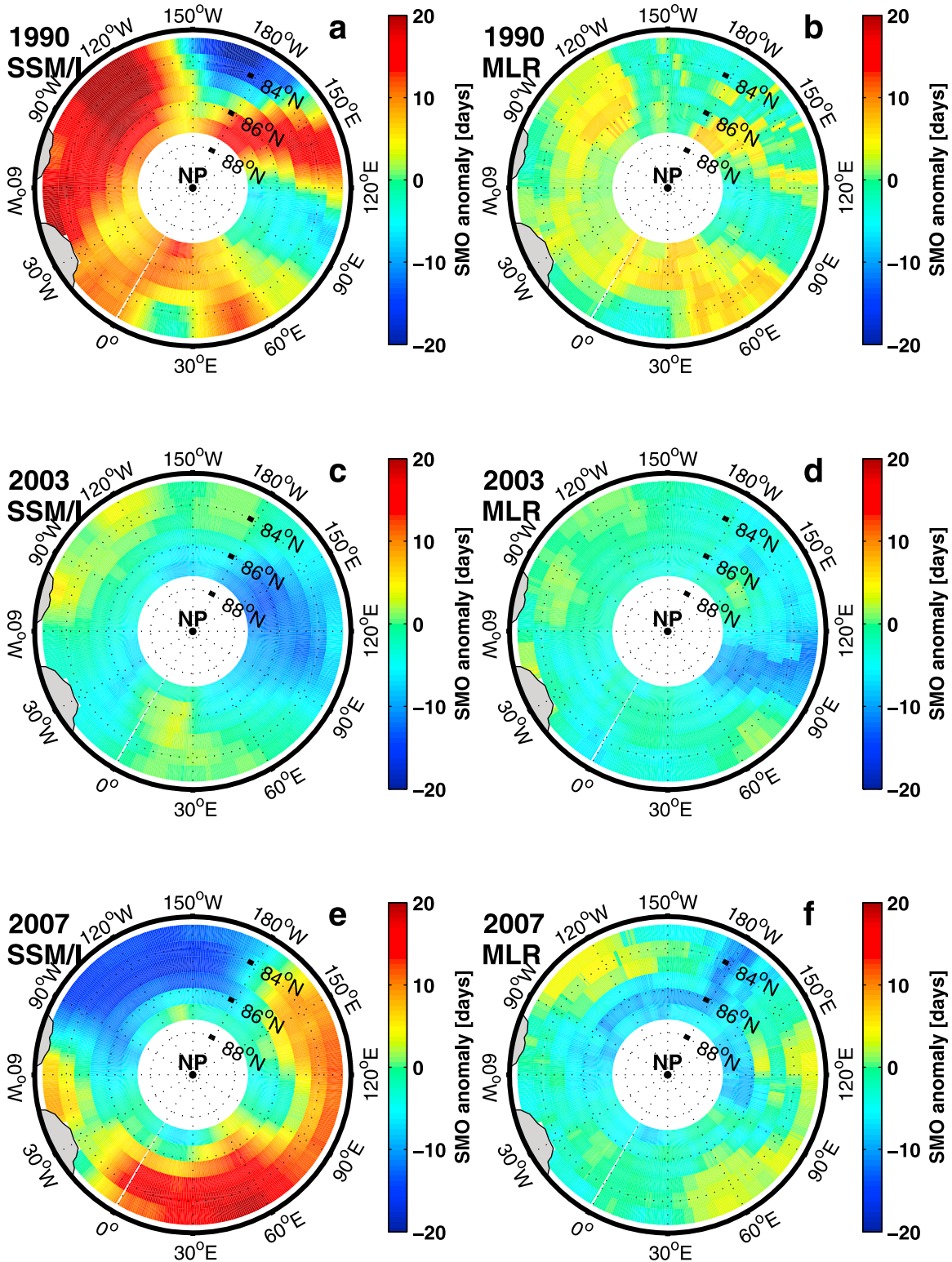


Figure 9. Comparison of the original SSM/I-based SMO time series (left-hand maps) versus the reconstructed SMO time series (right-hand maps) in (a, b) 1990, (c, d) 2003 and (e, f) 2007. SSM/I-based SMO anomalies (left-hand maps) are calculated relative to the 20-year local mean SMO date. The multilinear regression (MLR) equation from Table 1 and the local heat flux anomalies (5-day average, method M1) are applied to reconstruct SMO anomalies at each ERAI grid location.

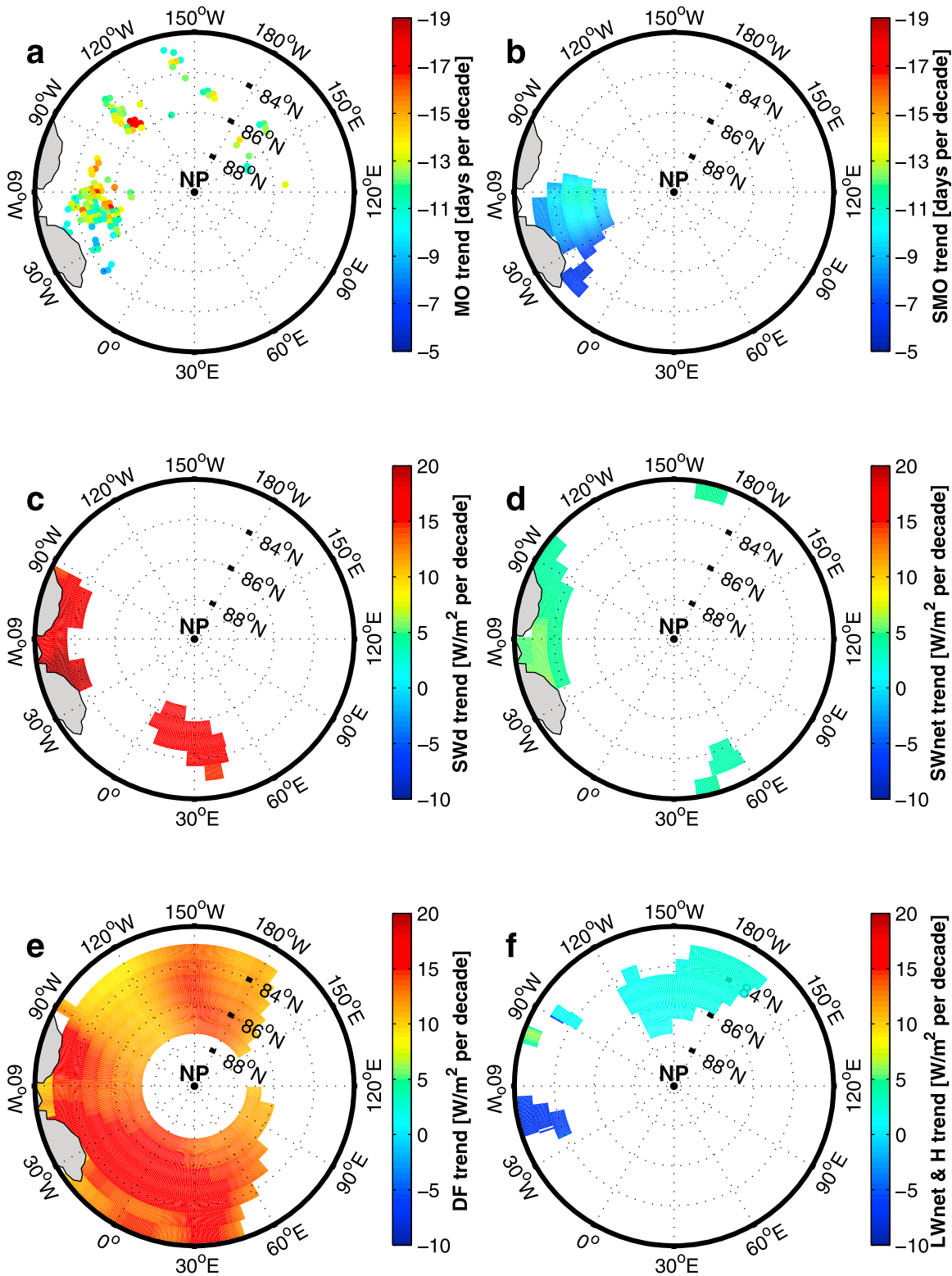


Figure 10. 20-year (1989–2008) local trends in (a) original MO data in 25 km resolution, (b) SMO in ERAI grid resolution, (c) SWd, (d) SWnet, (e) DF and (f) LWnet together with H. In Figure 10f dark blue represents LWnet trend, and light blue - green colors reflect H trend. Trends for ERAI surface fluxes are calculated based on the monthly mean heat fluxes in the same pre-melt period each year (20 April–21 May) and around the region. Trends were calculated only for the complete 20-year records, significant at $p < 0.01$.

LWd the most relevant time scale was 1–7 days, whereas for H and LE it was around 30–40 days. Yet, we note that significant r^2 were also found with other time averaging periods (Figure 5a, 5b, 6a, and 6b). The differences are probably related to the daily magnitudes of flux anomalies: NF and LWd reach larger magnitudes than LE and H and, accordingly, a long-term anomaly in LE and H is needed to cause a statistically significant effect on SMO.

[59] Over most of the central Arctic a combination of 2–4 fluxes explained SMO better than the individual fluxes alone or their sum (DR, DF and NF) (Figure 8c). This must be due to a different accuracy of the individual fluxes. However, if all fluxes were equally accurate in ERAI, NF should correlate with SMO better than any of its components or any combination of some of its components.

[60] The combination of LWd, SWd, LE and H anomalies (multilinear regression) well captures the spatial and interannual differences in SMO (Figures 7 and 9). Large SMO anomalies (of 15–35 days) and huge spatial differences in SMO (by 1–3 months within 50 km distances) are, however, poorly explained by surface fluxes. This is related to errors in fluxes (ERAI) and possibly also to the distinction of two sea ice types in the MO algorithm (SSM/I). The algorithm for MO detection applied by Markus *et al.* [2009] is different for the multiyear and first-year ice. We suspect that differences between ice types, most likely contribute to the interannual variations in SMO. Further studies are needed to find out how well surface fluxes explain SMO variance on top of different ice types.

[61] A detailed statistical investigation of the effect of snow and ice thickness and the conductive heat flux on SMO variance and trends would require data with spatial and temporal resolution comparable to ERAI, but no such data are currently available. We may, however, assume that the variability in the conductive heat flux was one of the main factors that reduced the capability of radiative and turbulent fluxes to explain SMO variance.

[62] The original MO record of Markus *et al.* [2009] is not fully independent of ERAI, because SSM/I data of sea ice concentration were applied in both. However, if focusing on the circumpolar central Arctic with a prescribed SIC of 100% in ERAI, and also extracting the SMO signal from the MO record, we can consider these data sets fully independent. In the future, the SMO data could be utilized to improve reanalyses by means of surface (skin) temperature assimilation. Regarding the hole at the North Pole and the spatial resolution, the active microwave time series of the backscatter [Kwok *et al.*, 2003] could be used to fill in the gap and to improve the spatial coverage of the existing MO records.

[63] Errors detected in ERAI near-surface air temperature and moisture during Arctic summer [Lüpkes *et al.*, 2010] and simplified SIC representation north of 83°N indicate that neither surface fluxes are free of errors. However, a good aspect in reanalysis is that the same model and data assimilation system were applied throughout the period, resulting in a spatially and temporally consistent data set. Errors in surface fluxes may, however, depend on weather and sea ice conditions, which could generate interannual variations in the errors, but such a possible dependence has not been investigated over Arctic sea ice yet. Furthermore it is unlikely that errors in the surface fluxes could generate artificially improved correlations between the fluxes and SMO. Instead

errors in surface heat fluxes, in MO detection, and SMO sampling (used as the reference date for the pre-melt period definition) should have increased the scatter in the observed relationship between SMO and the fluxes, thus reducing correlations.

[64] We also highlight that the *continuous* MO detected with the remote sensing by Markus *et al.* [2009] is an instance (Julian day) when either (a) liquid water remains on top of the sea ice (snow melt), or (b) the final sea ice divergence occurs. Although SMO and the ice divergence are closely related, they have a different origin. SMO on top of large and compact ice slab is due to a sufficient accumulation of the net heat flux (NF) within the snowpack, whereas opening of leads and polynyas (before melt ponds appear on top of sea ice) is due to divergent ice drift, typically caused by winds, tides, ocean currents of other origin, or bottom melt of ice. Studies on the latter processes are beyond the scope of this paper, but these aspects are essential for the treatment and interpretation of the original MO data. It seems that in the earlier analyses of satellite-based MO records, SMO and opening of leads and polynyas have not been distinguished.

[65] We presented quantitative SMO versus heat flux relationships only for the central Arctic (83–87°N), where it was possible to reliably detect the causal effect of surface fluxes on SMO. However, strong statistical relationships between SMO and surface fluxes were also found in the seasonal ice zone: Kara, Laptev, East-Siberian, Chukchi and eastern Beaufort Seas and the Baffin Bay. In these areas the most important fluxes were NF and SWnet. In contrast to the central Arctic (83–87°N) where ERAI surface fluxes were the least affected by SIC changes, in areas south of 83°N ERAI SIC dropped below 80% at least once during the pre-melt period (Figure 3f). As a result, when the ice concentration is reduced, the stronger SW absorption by the open water contributed to the additional NF accumulation. In other words, southward from 83°N, the positive NF and SWnet flux anomalies during the pre-melt period were due to the opening of leads or polynyas at least once within the 20-year record. Hence, some positive NF and SWnet flux anomalies were not a reason for the early SMO, and the statistically significant relationships were only partly due to the causal effect of fluxes on SMO. The effect of SIC on LWd was not as straightforward as in the case of NF and SWnet. Interannual LWd anomalies explained up to 70% of the local interannual SMO variance southward from 83°N, significant within vast areas of the northern Kara Sea, Laptev Sea, northward of the East-Siberian-Beaufort Seas (75–83N) and in the western Baffin Bay.

6. Conclusions

[66] Applying ERAI reanalysis of radiative and turbulent surface heat fluxes and satellite passive microwave (SSM/I) data of sea ice concentration and SMO in the period of 1989–2008, we evaluated the portion of the interannual variance in SMO explained by the surface fluxes over the central Arctic Ocean at 83–87°N. High and causally relevant correlations are found between the surface flux anomalies and SMO timing: a larger net heat flux and downward longwave radiation and weaker heat loss from the surface via the turbulent fluxes (LE and H) occur in springs/locations with an earlier SMO.

[67] The anomaly of the net heat flux 1–7 days prior the SMO explains up to 65% of the interannual variance in SMO. The main term of the net flux is the downward longwave radiation, which alone accounts for up to 90% of SMO variance over a limited area in western central Arctic. Solar radiation is not an important factor alone, but in combination with other fluxes improves the explained variance of SMO. Seasonal 30 to 40-day anomalies in the turbulent fluxes of sensible and latent heat explain locally up to 72% and 56% of the interannual SMO variance respectively. Regarding method M1, the individual heat fluxes and various combinations of them account for about 30–90% of the interannual SMO variance within as much as 68% of the study domain (Figure 8). When comparing all three methods (M1, M2 and M3) a significant explained variance in SMO timing is detected within 83.5% of the study domain (not shown).

[68] The downward longwave radiation is the most important flux term, best explaining the timing of SMO. This points out on the importance of clouds and air moisture. The difference in downward longwave radiation between overcast and clear skies is typically 70–100 W/m² [Beesley, 2000; Intrieri et al., 2002; Wang and Key, 2005]. It is, however, not only the cloud fraction and thickness that control longwave radiation, but also the phase of clouds; water clouds have a significantly higher longwave emissivity than ice clouds [Wang and Key, 2005; Pinto et al., 1997]. The association of an early SMO with a small heat loss from the surface by the turbulent fluxes of sensible and latent heat suggests that an early SMO is related to the presence of warm and moist air over the sea ice. Warm air advection is an important mechanism for synoptic-scale near-surface warming events over Arctic sea ice, and it is often associated with low-level liquid-phase clouds [Persson et al., 2002; Vihma and Pirazzini, 2005]. These are the conditions that favor both large downward longwave radiation and reduced turbulent heat loss from the surface, accordingly also favoring an early SMO.

[69] Local SMO gradients of up to one month per 50 km distance are occasionally related to large surface flux gradients (up to 25 W/m² in NF within 50 km distance) associated with the atmospheric fronts, and further should be examined together with the sea ice types. In agreement with the earlier SSM/I-based studies, the 20-year MO and SMO trends in the central circumpolar Arctic Ocean are toward earlier spring melt. Local MO and SMO trends of 13 and 9 days per decade, respectively, are found within a limited area where complete 20-year time series were available. SMO trends cannot be reasonably explained by ERAI surface fluxes. Moreover, we stress that the trend estimates strongly depend on the method applied and should be considered with caution.

[70] To reach these results, it was essential to extract the SMO signal out of the original MO record by Markus et al. [2009], which also includes cases of opening of leads and polynyas. The analysis based on three alternative methods (M1, M2, or M3) yields essentially similar results. While differences exist in detailed numerical values (r^2 , rmse, length of the best time averaging period), the main conclusions of the work do not depend on the method.

[71] We stress that more studies are needed to better understand and quantify the factors controlling SMO. A high priority should be given to the studies investigating the relationships between the sea ice, surface heat fluxes, local meteorological conditions (clouds, wind, air temperature and

humidity), cyclones, and large-scale circulation. In particular, the important role of downward longwave radiation on SMO calls for more studies on the cloud radiative forcing, sources of Arctic clouds (advection from lower latitudes versus evaporation from ice-free areas in the Arctic), and the evolution of cloud properties with changing sea ice cover. The results obtained may increase the potential for seasonal prediction of Arctic sea ice conditions. As the SMO initiates the albedo feedback process, the conditions favorable for early SMO are also favorable for larger ice melt and heat storage in the upper ocean [Perovich et al., 2007a, 2007b; Notz, 2009], and hence, for reduced sea ice cover and later freeze-up in the following fall.

[72] **Acknowledgments.** We are grateful to J. Stroeve, T. Markus and W. Meier for providing MO time series and the interaction during the study. We would like to thank our two reviewers, and also M. Tjernström, J. C. Gascard and T. Pleavin for very constructive and valuable suggestions, corrections and comments. This work was supported by the European projects DAMOCLES (Developing Arctic Modeling and Observing Capabilities for Long-term Environmental Studies, contract number 018509) and SEARCH for DAMOCLES (contract number 037111), both financed by the European Commission in the 6th Framework program. Those two projects were also IPY projects.

References

- Anderson, M. R. (1987), Snow melt on sea ice surfaces as determined from passive microwave satellite data, in *Large Scale Effects of Seasonal Snow Cover (Proceedings of the Vancouver Symposium, August 1987)*, IAHS Publ. 166, 329–342.
- Anderson, M. R., and S. D. Drobot (2001), Spatial and temporal variability in snowmelt onset over Arctic sea ice, *Ann. Glaciol.*, 33, 74–78, doi:10.3189/172756401781818284.
- Barber, E., T. N. Papakyriakou, and E. F. LeDrew (1994), On the relationship between energy fluxes, dielectric properties, and microwave scattering over snow covered first-year sea ice during the spring transition period, *J. Geophys. Res.*, 99(C11), 22,401–22,411, doi:10.1029/94JC02201.
- Beesley, J. A. (2000), Estimating the effect of clouds on the arctic surface energy budget, *J. Geophys. Res.*, 105(D8), 10,103–10,117, doi:10.1029/2000JD900043.
- Belchansky, G. I., D. C. Douglas, and N. G. Platonov (2004), Duration of the Arctic Sea ice melt season: Regional and interannual variability, 1979–2001, *J. Clim.*, 17, 67–80, doi:10.1175/1520-0442(2004)017<0067:DOTAS>2.0.CO;2.
- Bitz, C. M., and Q. Fu (2008), Arctic warming aloft is data set dependent, *Nature*, 455, E3–E4, doi:10.1038/nature07258.
- Bitz, C. M., D. S. Battisti, R. E. Moritz, and J. A. Beesley (1996), Low frequency variability in the Arctic atmosphere, sea ice and upper ocean climate system, *J. Clim.*, 9(2), 394–408, doi:10.1175/1520-0442(1996)009<0394:LFFVITA>2.0.CO;2.
- Cavalieri, D., C. Parkinson, P. Gloersen, and H. J. Zwally (1996), Sea ice concentration from Nimbus-7 SMMR and DMSP SSM/I passive microwave data, digital media, Natl. Snow and Ice Data Cent., Boulder, Colo. [Updated 2008.]
- Cheng, B., T. Vihma, R. Pirazzini, and M. Granskog (2006), Modeling of superimposed ice formation during spring snow-melt period in the Baltic Sea, *Ann. Glaciol.*, 44, 139–146, doi:10.3189/172756406781811277.
- Cheng, B., Z. Zhang, T. Vihma, M. Johansson, L. Bian, Z. Li, and H. Wu (2008), Model experiments on snow and ice thermodynamics in the Arctic Ocean with CHINARE 2003 data, *J. Geophys. Res.*, 113, C09020, doi:10.1029/2007JC004654.
- Dee, D. P., and S. Uppala (2009), Variational bias correction of satellite radiance data in the ERA-Interim reanalysis, *Q. J. R. Meteorol. Soc.*, 135(644), 1830–1841, doi:10.1002/qj.493.
- Dee, D. P., et al. (2011), The ERA-Interim reanalysis: Configuration and performance of the data assimilation system, *Q. J. R. Meteorol. Soc.*, 137, 553–597, doi:10.1002/qj.828.
- Drafer, N. R., and H. Smith (1998), *Applied Regression Analysis*, pp. 307–312, Wiley-Interscience, Hoboken, N. J.
- Drobot, S. D. (2007), Using remote sensing data to develop seasonal outlooks for Arctic regional sea-ice minimum extent, *Remote Sens. Environ.*, 111, 136–147, doi:10.1016/j.rse.2007.03.024.

- Drobot, S. D., and M. R. Anderson (2001), Comparison of interannual snowmelt-onset dates with atmospheric conditions, *Ann. Glaciol.*, *33*, 79–84, doi:10.3189/172756401781818851.
- Ebert, E. E., and J. A. Curry (1993), An intermediate one-dimensional thermodynamic sea-ice model for investigating ice-atmosphere interactions, *J. Geophys. Res.*, *98*(C6), 10,085–10,109, doi:10.1029/93JC00656.
- European Centre for Medium-Range Weather Forecasts (ECMWF) (2008a) Integrated Forecast System (IFS) documentation—Cy33r1. Part II: Data assimilation, Reading, U. K.
- European Centre for Medium-Range Weather Forecasts (ECMWF) (2008b), Integrated Forecast System (IFS) documentation—Cy33r1. Part IV: Physical processes, operational implementation, Reading, U. K.
- Ehn, J. K., M. A. Granskog, T. Papakyriakou, R. Galley, and D. G. Barber (2006), Surface albedo observations of Hudson Bay (Canada) land-fast sea ice during melt onset, *Ann. Glaciol.*, *44*, 23–29, doi:10.3189/172756406781811376.
- Eicken, H., and P. Lemke (2001), The response of polar sea ice to climate variability and change, in *Climate of the 21st Century: Changes and Risks*, edited by J. L. Lozan et al., pp. 206–211, Wiss. Auswertungen/GEO, Hamburg, Germany.
- Fiorino, M. (2004), A multi-decadal daily sea surface temperature and sea ice concentration data set for the ERA-40 reanalysis, *ERA-40 Proj. Rep. Ser. 12*, Eur. Cent. for Medium-Range Weather Forecasts, Reading, U. K.
- Forster, R. R., D. G. Long, K. C. Jezek, S. D. Drobot, and M. R. Anderson (2001), The onset of Arctic sea-ice snowmelt as detected with passive- and active-microwave remote sensing, *Ann. Glaciol.*, *33*, 85–93, doi:10.3189/172756401781818428.
- Giles, K. A., S. W. Laxon, and A. L. Ridout (2008), Circumpolar thinning of Arctic sea ice following the 2007 record ice extent minimum, *Geophys. Res. Lett.*, *35*, L22502, doi:10.1029/2008GL035710.
- Granskog, M., T. Vihma, R. Pirazzini, and B. Cheng (2006), Superimposed ice formation and surface energy fluxes on sea ice during the spring melt-freeze period in the Baltic Sea, *J. Glaciol.*, *52*(176), 119–127, doi:10.3189/172756506781828971.
- Grant, A. N., S. Bronnimann, and L. Haimberger (2008), Recent Arctic warming vertical structure contested, *Nature*, *455*, E2–E3, doi:10.1038/nature07257.
- Graversen, R. G., T. Mauritsen, M. Tjernstrom, E. Kallen, and G. Svensson (2008), Vertical structure of recent Arctic warming, *Nature*, *451*, 53–56, doi:10.1038/nature06502.
- Grenfell, T. C., and D. K. Perovich (1984), Spectral albedos of sea ice and incident solar irradiance in the southern Beaufort Sea, *J. Geophys. Res.*, *89*(C3), 3573–3580, doi:10.1029/JC089iC03p03573.
- Grenfell, T. C., and D. K. Perovich (2004), Seasonal and spatial evolution of albedo in a snow-ice-land-ocean environment, *J. Geophys. Res.*, *109*, C01001, doi:10.1029/2003JC001866.
- Intrieri, J., C. W. Fairall, M. D. Shupe, P. O. Persson, E. L. Andreas, P. S. Guest, and R. E. Moritz (2002), An annual cycle of Arctic surface cloud forcing at SHEBA, *J. Geophys. Res.*, *107*(C10), 8039, doi:10.1029/2000JC000439.
- Kwok, R., and D. A. Rothrock (2009), Decline in Arctic sea ice thickness from submarine and ACESat records: 1958–2008, *Geophys. Res. Lett.*, *36*, L15501, doi:10.1029/2009GL039035.
- Kwok, R., G. F. Cunningham, and S. V. Nghiem (2003), A study of melt over the Arctic Ocean in RADARSAT synthetic aperture radar data, *J. Geophys. Res.*, *108*(C11), 3363, doi:10.1029/2002JC001363.
- Laxon, S. W., N. Peacock, and D. Smith (2003), High interannual variability of sea ice thickness in the Arctic region, *Nature*, *425*, 947–950, doi:10.1038/nature02050.
- Lüpkes, C., T. Vihma, E. Jakobson, G. König-Langlo, and A. Tetzlaff (2010), Meteorological observations from ship cruises during summer to the central Arctic: A comparison with reanalysis data, *Geophys. Res. Lett.*, *37*, L09810, doi:10.1029/2010GL042724.
- Markus, T., J. C. Stroeve, and J. Miller (2009), Recent changes in Arctic sea ice melt onset, freeze up and melt season length, *J. Geophys. Res.*, *114*, C12024, doi:10.1029/2009JC005436.
- Nghiem, S., R. Kwok, D. Perovich, and D. Barber (2003), Impact of cloud cover on sea ice surface melt, paper presented at Seventh Conference on Polar Meteorology and Oceanography and Joint Symposium on High-Latitude Climate Variations, Am. Meteorol. Soc., Boston, Mass.
- Notz, D. (2009), The future of ice sheets and sea ice: Between reversible retreat and unstoppable loss, *Proc. Natl. Acad. Sci. U. S. A.*, *106*(49), 20,590–20,595, doi:10.1073/pnas.0902356106.
- Perovich, D. K., and B. Elder (2001), Temporal evolution and spatial variability of the temperature of Arctic sea ice, *Ann. Glaciol.*, *33*, 207–211, doi:10.3189/172756401781818158.
- Perovich, D. K., B. Light, H. Eicken, K. F. Jones, K. Runciman, and S. V. Nghiem (2007a), Increasing solar heating of the Arctic Ocean and adjacent seas, 1979–2005: Attribution and role in the ice-albedo feedback, *Geophys. Res. Lett.*, *34*, L19505, doi:10.1029/2007GL031480.
- Perovich, D. K., S. V. Nghiem, T. Markus, and A. Schweiger (2007b), Seasonal evolution and interannual variability of the local solar energy absorbed by the Arctic sea ice-ocean system, *J. Geophys. Res.*, *112*, C03005, doi:10.1029/2006JC003558.
- Persson, P. O. G., C. W. Fairall, E. L. Andreas, P. S. Guest, and D. K. Perovich (2002), Measurements near the Atmospheric Surface Flux Group Tower at SHEBA: Near-surface conditions and surface energy budget, *J. Geophys. Res.*, *107*(C10), 8045, doi:10.1029/2000JC000705.
- Pinto, J. O., J. A. Curry, and C. W. Fairall (1997), Radiative characteristics of the Arctic atmosphere during spring as inferred from ground-based measurements, *J. Geophys. Res.*, *102*, 6941–6952, doi:10.1029/96JD03348.
- Robinson, D. A., G. Scharfen, M. Serreze, G. Kukla, and R. Barry (1986), Snow melt and surface albedo in the Arctic basin, *Geophys. Res. Lett.*, *13*(9), 945–948, doi:10.1029/GL013i009p00945.
- Screen, J. A., and I. Simmonds (2011), Erroneous Arctic temperature trends in the ERA-40 reanalysis: A closer look, *J. Clim.*, *24*(10), 2620–2627, doi:10.1175/2010JCLI4054.1.
- Screen, J. A., and I. Simmonds (2012), Declining summer snowfall in the Arctic: Causes, impacts and feedbacks, *Clim. Dyn.*, *38*, 2243–2256, doi:10.1007/s00382-011-1105-2.
- Stone, R. S., D. C. Douglas, G. I. Belchansky, S. D. Drobot, and J. Harris (2005), Cause and effect of variations in western Arctic snow and sea ice cover, Paper 8.3 presented at Eighth Conference on Polar Oceanography and Meteorology, Am. Meteorol. Soc., San Diego, Calif.
- Stroeve, J., T. Markus, W. N. Meier, and J. Miller (2006), Recent changes in the Arctic melt season, *Ann. Glaciol.*, *44*(1), 367–374, doi:10.3189/172756406781811583.
- Thiébaux, J., E. Rogers, W. Wang, and B. Katz (2003), A new high-resolution blended real-time global sea surface temperature analysis, *Bull. Am. Meteorol. Soc.*, *84*, 645–656, doi:10.1175/BAMS-84-5-645.
- Thorndike, A., and R. Colony (1982), Sea ice motion in response to geostrophic winds, *J. Geophys. Res.*, *87*(C8), 5845–5852, doi:10.1029/JC087iC08p05845.
- Thorne, P. W. (2008), Arctic tropospheric warming amplification?, *Nature*, *455*, E1–E2, doi:10.1038/nature07256.
- Uppala, S., D. Dee, S. Kobayashi, P. Berrisford, and A. Simmons (2008), Towards a climate data assimilation system: Status update of ERA Interim, *ECMWF Newsl.* *115*, pp. 12–18, Eur. Cent. for Medium-Range Weather Forecasts, Reading, U. K.
- Vihma, T., and R. Pirazzini (2005), On the factors controlling the snow surface and 2-m air temperatures over the Arctic sea ice in winter, *Boundary Layer Meteorol.*, *117*(1), 73–90, doi:10.1007/s10546-004-5938-7.
- Vihma, T., M. M. Johansson, and J. Launiainen (2009), Radiative and turbulent surface heat fluxes over sea ice in the western Weddell Sea in early summer, *J. Geophys. Res.*, *114*, C04019, doi:10.1029/2008JC004995.
- Wang, X., and J. R. Key (2005), Arctic surface, cloud, and radiation properties based on the AVHRR Polar 36 Pathfinder dataset. Part I: Spatial and temporal characteristics, *J. Clim.*, *18*(14), 2558–2574, doi:10.1175/JCLI3438.1.
- Yackel, J. J., D. G. Barber, T. N. Papakyriakou, and C. Breneman (2007), First-year sea ice spring melt transitions in the Canadian Arctic Archipelago from time-series synthetic aperture radar data, 1992–2002, *Hydrol. Processes*, *21*, 253–265, doi:10.1002/hyp.6240.
- Zhang, J., K. Stamnes, and S. A. Bowling (1996), Impact of clouds on surface radiative fluxes and snow melt in the Arctic and sub Arctic, *J. Clim.*, *9*(9), 2110–2123, doi:10.1175/1520-0442(1996)009<2110:IOCCOSR>2.0.CO;2.
- Zhang, T., S. A. Bowling, and K. Stamnes (1997), Impact of the atmosphere on surface radiative fluxes and snowmelt in the Arctic and Subarctic, *J. Geophys. Res.*, *102*(D4), 4287–4302, doi:10.1029/96JD02548.
- Zuidema, P., B. Baker, Y. Han, J. Intrieri, J. Key, P. Lawson, S. Matrosov, M. Shupe, R. Stone, and T. Uttal (2005), An Arctic springtime mixed-phase cloudy boundary layer observed during SHEBA, *J. Atmos. Sci.*, *62*(1), 160–176, doi:10.1175/JAS-3368.1.